OXFORD

The Origin and Evolution of DMM-Like Lithospheric Mantle Beneath Continents: Mantle Xenoliths from the Oku Volcanic Group in the Cameroon Volcanic Line, West Africa

Jacek Puziewicz [ID][1,*], Sonja Aulbach [ID][2], Mary-Alix Kaczmarek[3], Theodoros Ntaflos[4], Axel Gerdes[2], Hubert Mazurek[1], Anna Kukuła[5],

Magdalena Matusiak-Małek[1], Sylvin S. T. Tedonkenfack[1] and Małgorzata Ziobro-Mikrut[1]

[1]Faculty of Earth Sciences and Environmental Management, Institute of Geological Sciences, University of Wroclaw, Wroclaw, Poland
[2]Goethe University Frankfurt am Main, Institute for Geosciences and Frankfurt Isotope and Element Research Center (FIERCE), Frankfurt, Germany
[3]Géosciences Environnement Toulouse (GET), Observatoire Midi-Pyrénées CNRS-CNES-IRD-Université Toulouse III, Toulouse, France
[4]Department of Lithospheric Research, University of Vienna, Vienna, Austria
[5]Polish Academy of Sciences, Institute of Geological Sciences, Warsaw, Poland

*Corresponding author: E-mail: jacek.puziewicz@uwr.edu.pl

Abstract

The lithospheric mantle as sampled by peridotite xenoliths in some continental settings resembles the source of mid-ocean ridge basalts (MORB). Whether this resemblance is a primary feature or the result of post-formation secondary processes remains controversial. Here, the age, origin and thermochemical evolution of fertile continental mantle are constrained based on the chemical composition of minerals in spinel-facies lherzolite and websterite xenoliths from the Wum maar and Befang cinder cone of the Oku Volcanic Group (Cameroon Volcanic Line, West Africa), combined with *in-situ* Sr isotope compositions of clinopyroxene and fabric investigation by Electron Backscatter Diffraction (EBSD). The majority of lherzolites (here assigned to Group I) consist of minerals with fertile composition (olivine Fo89, Al-rich pyroxenes, spinel Cr# 0.08–0.10). Clinopyroxene is LREE-depleted and has depleted $^{87}Sr/^{86}Sr$ (0.7017–0.7020). Crystal-preferred orientation determined by EBSD reveals that clinopyroxene, and sporadically both clino- and orthopyroxene, post-date the olivine framework. Subordinate Group II lherzolites also contain secondary clinopyroxene which is LREE-enriched and has higher $^{87}Sr/^{86}Sr$ (0.7033). In contrast, the scarce lherzolites of Group III are more refractory: they contain 72–78 vol.% olivine, Al-poor pyroxenes, and spinel with Cr# 0.18. Clinopyroxene ($^{87}Sr/^{86}Sr$ 0.7021) is texturally coeval with olivine and orthopyroxene. Few lherzolites contain amphibole ($^{87}Sr/^{86}Sr$ 0.7031) which post-dates the nominally anhydrous minerals. Most of the websterites (Group A) are aluminous (spinel Cr# 0.04–0.06) with LREE-depleted clinopyroxene having depleted $^{87}Sr/^{86}Sr$ ratios (0.7017–0.7020) similar to Group I lherzolites. Chemical characteristics of minerals coupled with the crystal-preferred orientation data suggests that Group I lherzolites originated in the spinel stability field by reactive intergranular percolation of an incompatible element-depleted MORB-like melt. Group A websterites likely formed as cumulates from that melt. The Group II lherzolites supposedly occur close to lithosphere-asthenosphere boundary and record interaction with lavas of the Cameroon Volcanic Line, whereas Group III lherzolites occur in the shallow part of the mantle profile and represent the protolith from which the Group I lherzolites were formed. Local crystallization of amphibole and concomitant recrystallization of the host lherzolite were driven by supply of water in an event post-dating the formation of LREE-depleted rejuvenated rocks. Migration of alkaline melts of the CVL apparently did not significantly affect the mineral and chemical composition of the lithospheric mantle, which allowed Group I lherzolites and Group A websterites to retain very low $^{87}Rb/^{86}Sr$ (average 0.002) and depleted $^{87}Sr/^{86}Sr$ ratios in clinopyroxene. This not only indicates their formation in the Paleoproterozoic (~2.0–2.25 Ga), possibly during the Eburnean orogeny at the margin of the Congo craton, but also indicates surprisingly little influence of the regionally recognized Pan-African event.

Keywords: Cameroon Volcanic Line, depleted melt, refertilization, subcontinental lithospheric mantle, DMM

INTRODUCTION

Lithospheric plates consist mainly of mantle rocks, but because these rocks only occur at sub-Moho depths, direct sampling is almost never possible. Within continents, geological knowledge about the lithology and the evolution of lithospheric mantle is accumulated by bringing together fragmentary information yielded by studies of xenoliths brought to the surface, typically by alkaline volcanic rocks, and of tectonically exhumed mantle fragments embedded in crustal orogenic sequences (e.g. Nixon, 1987; Bodinier & Godard, 2003; Pearson *et al.,* 2003).

The lithospheric mantle underlying oceans is residual after decompression melting of asthenosphere upwelled beneath ocean rifts (e.g. Niu, 1997) and its source is characterized by a mild depletion in incompatible elements (Salters & Stracke, 2004; Workman & Hart, 2005). Though affected by melt-rock reactions (e.g. Warren & Shimizu, 2010 ; Warren, 2016), recycling of oceanic

lithosphere at plate margins after few hundred million years at most implies a relatively short-lived and therefore simple evolution. By contrast, long-lived continental mantle roots usually have a more complicated history, commencing with one or more episodes of melt extraction, often followed by multiple metasomatic events, giving rise to distinct incompatible element enrichment, introduction of metasomatic minerals and/or to refertilization (e.g. Pearson *et al.,* 2003, 2014; O'Reilly & Griffin, 2013). Refertilization may be so severe that the affected mantle volume becomes almost indistinguishable from an undepleted source rock, an example being the lherzolites from their type locality in the Lherz Massif (e.g. Le Roux *et al.,* 2007). As a consequence, continental lithospheric mantle from some locations resembles a depleted mid-ocean ridge basalts (MORB)-source. Its occurrences are documented, for example, by xenoliths from Tariat in Mongolia (Carlson & Ionov, 2019), Massif Central in France (Lenoir *et al.,* 2000) and Oku Volcanic Group in Cameroon (Tedonkenfack *et al.,* 2021). The refertilized depleted MORB mantle (DMM)-like continental mantle is characterized by fertile major element mineral compositions coupled with depletion in the most incompatible trace elements like light REE (e.g. Tedonkenfack *et al.,* 2021).

Carlson & Ionov (2019) suggested that mantle with these characteristics results from the accretion of slices of oceanic mantle to the continent root, which remained undisturbed thereafter, and a detailed model of the accretion mechanism was presented by Scott *et al.* (2019). Alternatively, reactive percolation of melt chemically similar to MORB can modify subcontinental lithospheric mantle such that it resembles its oceanic counterpart. This concept was first proposed by Lenoir *et al.* (2000) in their study of mantle xenoliths occurring in the French Massif Central. The newly formed rocks have the composition of lherzolite and were termed 'secondary lherzolites' by these authors. The geodynamic implications, in terms of the origin and subsequent stability of deep continental lithosphere, are significantly different, but unambiguous evidence is difficult to come by. One of the reasons is that both, the primary lherzolites formed by extraction of small volumes of melt from the asthenosphere and the secondary lherzolites formed by MORB-like melt percolation in lithospheric rocks, would contain clinopyroxene which is Al-rich and LREE-depleted. To obtain definitive arguments if this mineral is residual or newly formed, its position in the mineral crystallization sequence must be defined.

In this paper we present a model for the origin of DMM-like mantle occurring in subcontinental setting. We show the effects of MORB-like melt percolation on the lithospheric mantle and we characterize the nature of this melt based on the elemental and isotopic fingerprint it leaves in the affected rock volume. Our example comes from the Oku Volcanic Group in the Cameroon Volcanic Line in West Africa. We present new data on the mantle xenolith suite from the Wum maar and pair them with an expanded data set from the xenolith suite of the neighboring Befang cinder cone (Tedonkenfack *et al.,* 2021). To decipher the sequence of events which formed the lithospheric mantle beneath the Oku Volcanic Group, we use chemical analyses of major and trace elements in minerals, crystallographic preferred orientation study and $^{87}Sr/^{86}Sr$ ratios determined *in situ* in clinopyroxene and in amphibole.

GEOLOGICAL CONTEXT
Cameroon volcanic line

The Cameroon Volcanic Line (CVL) is a linear chain of volcanoes situated in the western part of the African continent and the adjacent part of the Atlantic Ocean. The volcanoes stretch NE–SW from the Biu and Adamawa Plateaus in Nigeria and Cameroon to the Pagalu Island in the Gulf of Guinea (Fig. 1). Volcanic activity in the CVL started in the early Eocene (52 Ma, Njome & de Wit, 2014) and continued to the Recent. The volume of the CVL lavas is small and they are mostly alkaline (Fitton, 1980), varying in composition from basanite to hypersthene-normative basalt (Njome & de Wit, 2014). Volcanoes located in the continental part of the CVL commonly are bimodal and also include trachytic, trachyphonolitic, rhyolitic and rare phonolitic lavas (Njome & De Wit, 2014). Some of the lavas carry xenoliths of peridotites and pyroxenites, which allow insights into the lithospheric mantle underlying the CVL.

The Oku Volcanic Group (OVG) is one of the four major volcanic centers in the continental sector of the CVL (Fig. 1). It is located at 9°54' - 10°50' E, 6°00' - 6°40' N, and consists of four stratovolcanoes (Mts. Oku, Babanki, Nyos and Nkambe); Mt. Oku is the highest of them (3011 m asl). The Oku volcanic activity lasted from 30 to <1 Ma (Njome & de Wit, 2014). Lava compositions vary from basanite to trachyte and rhyolite (Asaah *et al.,* 2015). Asaah *et al.* (2021) showed that most (> 85%) of the mafic lavas from the OVG which are <12 Ma, come from an asthenospheric source and have a HIMU signature.

Crust and lithospheric mantle underlying CVL

The CVL is located on the metamorphic-igneous basement of the Central African Orogenic Belt (CAOB; Fig. 1). The Cameroon section of the CAOB comprises the Northern Domain, the Adamawa-Yade Domain and the Southern Domain (Fig. 1; Tchakounté *et al.,* 2017; Toteu *et al.,* 2022). The Northern Domain forms the basement of the CVL. This Domain consists of Neoproterozoic volcanic and sedimentary rocks, which are intruded by 780–560 Ma calc-alkaline plutons (Tchakounté *et al.,* 2017 and references therein). The rocks of the Adamawa-Yade Domain are Paleoproterozoic to Archean in age. The Southern Domain consists of a Neoproterozoic nappe stack overlying the margin of the Congo Craton (Fig. 1; Tchakounté *et al.,* 2017 and references therein). Toteu *et al.* (2022) define also the Nyong-Bayomen Domain, interpreted by them to be a Paleoproterozoic nappe complex, which represents the SW continuation of the Adamawa-Yade Domain (Fig. 1). The Congo craton is located to the south of the Cameroon section of the CAOB, and the Benue Trough to the north (Fig. 1). The latter is an aborted rift which originated during the late Cretaceous opening of the southern Atlantic (e.g. Min & Hou, 2019).

The CAOB originated by the collision of the Congo Craton with the Sahara Craton at the time of Gondwana assembly (Neoproterozoic 'Panafrican' orogeny; Abdelsalam *et al.,* 2002). It is a part of the Brasiliano-Damara orogen of Western Gondwana (Cawood *et al.,* 2021). The Adamawa-Yade Domain is considered to be a part of the Eburnean (2.1–2.0 Ga) orogen formed during collision of São-Francisco and Congo Cratons (Tchouankoue *et al.,* 2021 and references therein), or a microcontinental terrain docked to the passive margin of the Congo Craton during the Panafrican collision (e.g. Bouyo *et al.,* 2015; Tchakounté *et al.,* 2017 and references therein). The Sahara craton was remobilized and the term 'Sahara metacraton' (Abdelsalam *et al.,* 2002; Sobh *et al.,* 2020) is commonly used.

Goussi Ngalamo *et al.* (2017) interpreted gravity data to show the Moho beneath the Oku Volcanic Group (OVG) at 38–40 km. The lithosphere-asthenosphere boundary (LAB) is located between 150 and 200 km beneath the Congo Craton (Goussi Ngalamo *et al.,* 2018). Beneath the Central African Orogenic Belt, the LAB shallows
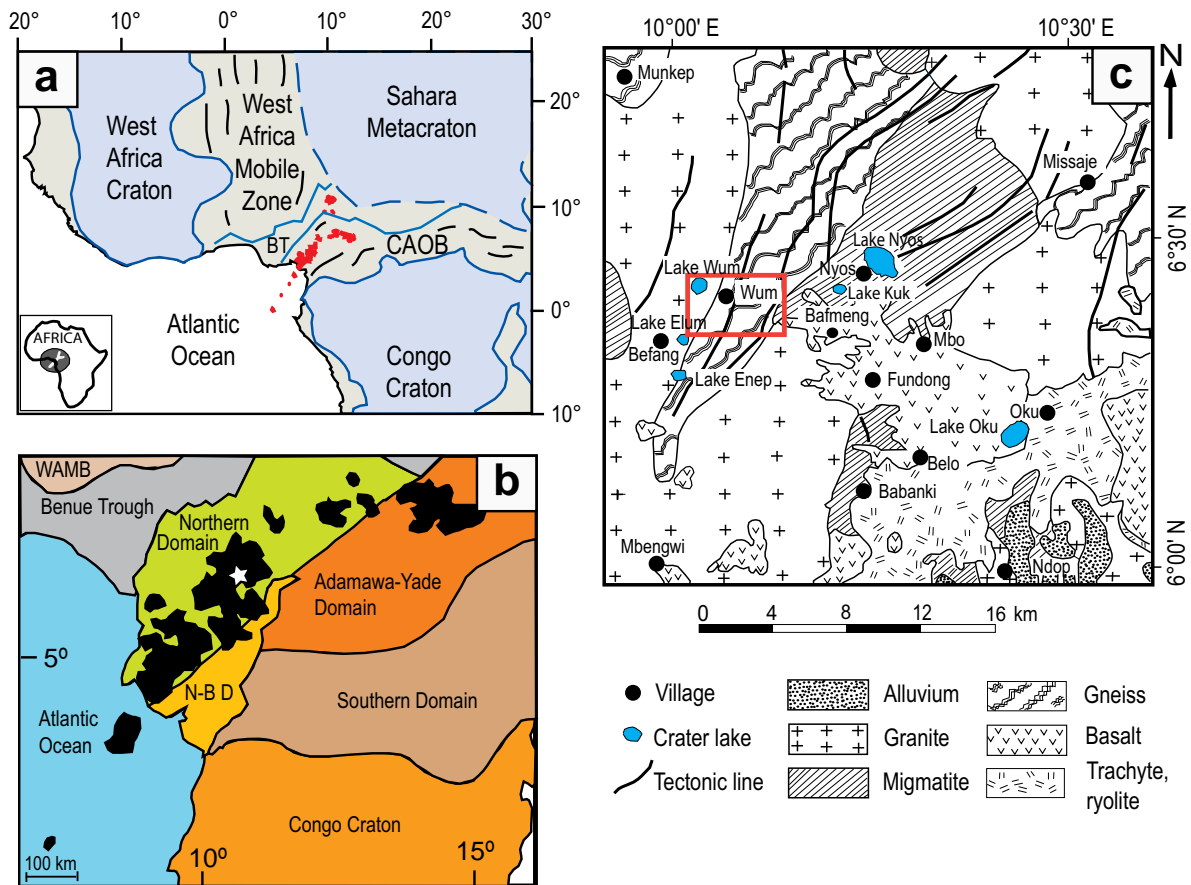
Fig. 1. (a) Location of the CVL (red) relative to major geological units of the basement of the western part of Africa. CAOB, Central African Orogenic Belt; BT, Benue Trough. The sketch is based on Tectonic Map of Africa (Milesi *et al., 2010*). (b) Major tectonic units between Congo Craton and Benue Trough and outcrops of lavas of the CVL (unit borders based on map of Toteu *et al., 2022*; lavas after Déruelle *et al., 2007*). Oku Volcanic Group marked by white star. WAMB, Western Africa Mobile Belt; N-B D, Nyong-Bayomen Domain. White denotes Cenozoic sedimentary rocks. (c) The location of the Wum maar ('Lake Wum') in the detailed geological map of the Oku region (after Asaah *et al., 2015*).

to ca. 110 km, and further to ca. 85–90 km beneath the OVG (Goussi Ngalamo *et al., 2018*). The lithosphere beneath the CVL exhibits no evidence for extensive melting in the crust or addition of mafic intrusions to lower/middle crust by underplating, which suggests no increased potential temperatures in the mantle, and lava generation by a low melt-producing mechanism like shear zones or delamination (Gallacher & Bastow, 2012). On the other hand, the seismic tomographic study of Reusch *et al.* (2010) shows a vertical tabular low velocity zone (LVZ) in the mantle beneath the CVL, which reaches a depth of over 300 km. The SE side of this LVZ is vertical, whereas the NW side is not well resolved, but is supposedly vertical down to 300 km (Reusch *et al.,* 2010). This LVZ can be due to thermal or compositional anomaly, rock anisotropy or the presence of melt/fluid, but Reusch *et al.* (2010) attribute it to a thermal perturbation, which thus must be ca. 280 K higher relative to the surrounding mantle.

Tomographic seismic models of O'Reilly *et al.* (2009) and Fishwick (2010) suggest that the upper mantle underlying the CVL forms a NE–SW corridor between the Congo and Western Africa cratons. These models, albeit crude, suggest that the lithospheric/asthenospheric mantle analogous to that underlying the continental part of the CVL stretches to the SW beneath the Gulf of Guinea and underlies the Atlantic part of the CVL.

Lithospheric mantle xenoliths occur abundantly in the lavas of the OVG. Most researchers suggested that they come from a lithospheric mantle domain which was affected by melt depletion followed by silicate or mixed silicate-carbonatite melt metasomatism (Temdjim, 2012; Pintér *et al.*, 2015; Liu *et al.*, 2017; Liu *et al.*, 2020). Liu *et al.* (2020) suggested they dated melt depletion in lherzolite xenoliths from Lake Nyos at ∼2.0 Ga. They used Lu-Hf isochron and Os 'aluminochron' ages as well as Re-depletion ages to argue that melt metasomatism occurred right after melt extraction. In contrast, the study of Liu *et al.* (2017) suggests a model depletion age of ca. 2.6 Ga using $^{187}Os/^{188}Os$-Al_2O_3 relationships. Based on the vicinity to the Congo craton, an Archean age is plausible, and the issue remains unresolved as the age arrays and model ages of both studies are subject to interpretation. Work by Tedonkenfack *et al.* (2021) indicates that lherzolites from nearby Befang site were affected by metasomatism by MORB-like melt derived from a Depleted MORB Mantle (DMM)-like source, with late addition of clinopyroxene constrained from crystal-preferred orientation analysis.

SAMPLING, ANALYTICAL METHODS AND TERMINOLOGY
Sampling and analytical methods applied

For this study we collected 43 xenoliths in the Wum maar. After macroscopic examination and exclusion of weathered specimens, we selected 19 samples for detailed study.

Petrographic sections of 100 μm thickness were used for detailed rock description and in-situ analyses. Ideally, the

Table 1: Mineral abundances in rocks from the Wum xenolith suite (vol.%)

Sample	Olivine	Orthopyroxene	Clinopyroxene	Spinel	Amphibole	Comments
H71	60.7	22.4	13.5	2.4	1.0	
H46	57.9	23.5	15.6	2.9	0.1	
H54	47.0	37.1	13.4	2.5		Opx max. 4 mm across
H41	51.6	34.1	13.4	0.9		Opx porphyroclasts max. 4 × 2.5 mm
HX2	67.4	23.2	8.5	0.9		Opx rectangular grains max. 6 × 3 mm
H42	54.2	28.5	13.3	4.0		
H55	55.0	29.3	12.9	2.8		Opx porphyroclasts max. 4 × 2.5 mm
H63	72.1	22.1	4.8	1.0		
H64	63.5	26.6	6.9	3.0		
HX1	67.7	21.3	9.9	1.1		Opx rectangular grains max. 6.5 × 4 mm
H47	58.2	22.3	15.3	4.2		
H13	71.9	19.3	7.0	1.8		Opx max. 2.5 mm across
H53	77.5	12.4	8.0	2.1		
H69	74.9	14.2	6.8	0.2	3.9	
H39	-	64.8	33.9	1.3		Opx porphyroclasts 12–15 mm
H43	13.1	31.7	54.2	1.0		Cpx porphyroclasts 10 mm
H65	5.4	58.2	28.5	7.9		
H50	26.1	30.1	36.7	7.1		Almost monomineral layers Opx porphyroclasts max. 6 × 4 mm Spinel porphyroclasts max. 4 × 9 mm
H60	-	23.5	60.9	15.6		Opx rectangular grains and porphyroclasts max. 6.5 × 3 mm Spinel porphyroclasts max. 8 × 4 mm

Opx, orthopyroxene; Cpx, clinopyroxene

sections should be cut perpendicular to the foliation and parallel to the lineation of the studied sample. The foliation was difficult to be unequivocally defined in the studied xenoliths, and lineation was not recognizable macroscopically. In consequence, many of the sections are not cut according to these requirements.

Some of the xenoliths, even if not weathered, are friable. Because of this, the sections show local embrittlement, which was unavoidable during their preparation.

Modal compositions (Table 1) were determined based on phase maps of thick sections made by Electron Backscatter Diffraction (EBSD) or by Scanning Electron Microscope (SEM). The volume of orthopyroxene may be overestimated in websterites when present as 10–15 mm porphyroclasts, because the standard 28 x 48 mm sections that we use are too small to be representative for these coarse-grained samples.

The chemical composition of minerals was analyzed by Electron Probe Microanalysis (EPMA, 'electron microprobe'; major elements) and by Laser Ablation –Inductively Coupled Plasma-Mass Spectrometry (LA-ICP-MS; trace elements). Crystal-preferred orientation (CPO) was studied by the EBSD technique in 10 rocks, and $^{87}Sr/^{86}Sr$ compositions in clinopyroxene were analyzed *in situ* by LA-ICP-MS in all studied samples and in amphibole in one sample. For comparative purposes we also studied in situ $^{87}Sr/^{86}Sr$ in clinopyroxene in a xenolith suite from the nearby Befang cinder cone, which was described recently in a separate study (Tedonkenfack et al., 2021).

Electron microprobe analyses

Mineral major element contents were analyzed by a Cameca SXFive FE electron microprobe at the Department of Lithospheric Research, University of Vienna, Austria. We applied an acceleration voltage of 15 kV and beam current of 20 nA. Counting times of 20 s were used on peak position and 10 s on background, except Ca and Ni in olivine (60 s on peak and 30 s on background) and Ni in

pyroxenes (30 s on peak and 15 s on background), which improved detection limits. The analytical setup for olivine included Ti, Al and Cr. We analyzed the Wum sections in two analytical sessions differing slightly by microprobe configuration (due to machine recalibration in each session), which resulted in small differences in detection limits. The detection limits for elements which occur in minor amounts are listed in Electronic Supplementary Material 1. We analyzed at least 5–10 grains of each mineral in thick section, at 2–4 points for some of these grains to assess homogeneity (Electronic Supplementary Material 1).

LA-ICP-MS analyses

Trace element contents in clinopyroxene, orthopyroxene and amphibole (if present) were analyzed by LA-ICP-MS at the Institut für Geowissenschaften, Goethe Universität Frankfurt (Frankfurt am Main, Germany). For this, the RESOlution (Resonetics) 193 nm ArF Excimer Laser (CompexPro 102, Coherent), operated at a laser energy of 5 J/cm^2 and repetition rate of 8 Hz was coupled to a Thermo Scientific Element XR ICP-MS. Sample runs were bracketed by measurements of NIST 612 glass, which was used for sensitivity calibration (reference values of Jochum et al., 2011, were applied). The Si content analyzed by electron microprobe was used as internal standard. The spot diameter was 50 (clinopyroxene) or 75 (orthopyroxene) μm. Basalt glasses BIR-1G and BCR-2G were used to monitor accuracy. Raw data were processed with the Glitter 4.0 software (van Achterberg et al., 2001). The reproducibility of BIR-1G was 5% or better for most elements (except Th and U ≤ 8%). Since the measured values of many elements of interest were low by 10–20% in comparison to accepted values, a correction factor was applied to the unknowns and to BCR-2G to validate the procedure. Trace element abundances for the corrected BCR-2 agree with accepted values within 5%, except Rb, Sr and Gd (≤ 10%). Results for samples and reference materials measured as unknowns are reported in Electronic Supplementary Material 2.

We typically analyzed 5–10 grains of both ortho- and clinopyroxene in each thick section (Electronic Supplementary Material 2). If the grain size allowed, 2 or 3 points in different parts of grains were analyzed (margin, center and one point between). This was commonly possible with orthopyroxene grains, whereas clinopyroxene grains typically were too small to allow multiple analyses. The location of individual spots is reported in Electronic Supplementary Material 2. Trace element and REE contents were normalized to Primitive Mantle (PM) using values of McDonough & Sun (1995).

The REE patterns of clinopyroxene are identical within uncertainty at the scale of individual grains and of multiple grains within a sample (Electronic Supplementary Material 3). Exceptions are lherzolites H63 and H64, the REE patterns of which differ slightly between La and Eu (for H64 see Electronic Supplementary Material 3). Trace element patterns of clinopyroxene further exhibit variations in contents of highly incompatible elements which are present in ultralow concentrations and consequently most sensitive to analytical uncertainties (Rb, Ba, Th, U, Nb, Ta); Rb is below the detection limit in many samples. The same applies to orthopyroxene in most samples. The variation in REE contents is slightly greater from La to Sm or Eu in orthopyroxene (for example see Electronic Supplementary Material), but is also taken to reflect scatter caused by the mass spectrometer working at the limits of detection.

Orthopyroxene porphyroclasts in websterites have clear rims, whereas the centers in many grains contain lamellae of clinopyroxene. The spacing of lamellae varies from few to few hundreds of micrometers, and their thickness from <1 μm to few tenths of μm. Even if the lamellae spacing is greater than the size of ablation crater, their oblique dip relative to the section surface (depending on how sections were cut) results in co-ablation of host and lamellae. This increases the contents of LREE in centers, and this kind of analyses was excluded as contaminated. An example is shown in Electronic Supplementary Material 3. In some samples, single analytical points in both ortho- and clinopyroxene yield compositions, that depart from the majority of analyses. They show no systematic location relative to grain margins/centers, and we assume that they are due to contamination of analyzed spots by optically invisible alteration-filled cracks or clino- or orthopyroxene lamellae and/or intergrowths and exclude them from the averages.

If the contaminated analyses are excluded, some of the remaining analytical variations likely reflect measurement uncertainty for highly incompatible elements, and true heterogeneity for less incompatible ones. Because of the overall homogeneity, we present averages for each sample in the following. The full set of LA-ICP-MS analytical data is presented in Electronic Supplementary Material 2, in which relative standard deviation of multiple analyses of each element in a sample is included. Since multiple spots per grain and multiple grains per sample were analyzed, this indicates whether there is homogeneity both at the grain and the sample scale and allows outliers to be identified.

In situ ^{87}Sr/^{86}Sr analyses of clinopyroxene

The same laser instrument used for trace element analyses, but linked to the Thermo-Finnigan Neptune Plus multi-collector (MC) ICP-MS, was used to determine Sr isotopes, also at the Institut für Geowissenschaften, Goethe Universität (Frankfurt am Main, Germany). The setup included the use of Faraday Cups in static collection mode, spot sizes of 85 or 108 μm (depending on grain size), and a 10 Hz repetition rate. Soda-lime glass SRM-NIST 610 was analyzed at the beginning of the analytical session to

empirically determine the mass bias for ^{87}Rb/^{85}Rb, yielding the ^{87}Rb/^{86}Sr required for accurate correction of the isobaric interference of ^{87}Rb on ^{87}Sr (analytical details in Aulbach *et al.,* 2016). Further, two basaltic reference materials (BCR-2G and BHVO-2) and a homogeneous in-house plagioclase standard (MIR-A) were run at the beginning and the end and interspersed during the sequence, to monitor precision and accuracy.

The ^{87}Sr/^{86}Sr results for these materials are 0.704978 ± 0.000062 (1σ, n = 14) for BCR-2G, 0.703571 ± 0.000025 (1σ, n = 14) for BHVO-2 and 0.703165 ± 0.000012 (1σ, n = 13) for MIR-A1, the latter just agreeing within uncertainty with the TIMS-derived ^{87}Sr/^{86}Sr of 0.703096 ± 0.000050 (Rankenburg, 2002). Therefore, values normalized to MIR-A are used in this study, deteriorating results for BCR-2G to ^{87}Sr/^{86}Sr of 0.704909 (compared with the GeoReM-preferred ^{87}Sr/^{86}Sr of 0.705003 ± 0.00004) and improving ^{87}Sr/^{86}Sr for BHVO-2 to 0.703502 (compared with GeoReM-preferred ^{87}Sr/^{86}Sr of 0.703469 ± 0.000007; http://georem.mpch-mainz.gwdg.de). It is worth emphasizing that the ^{87}Rb/^{86}Sr of peridotitic clinopyroxene analyzed in this study (average 0.0019 ± 0.0053 1σ for 24 samples in total) is, with the exception of a single sample (BFA13) with 0.026, far below that of the basalt glasses (0.39 for BCR-2 and 0.065 for BHVO-2), requiring insignificant corrections for the isobaric interference of ^{87}Rb on ^{87}Sr. In view of this, the results for the peridotitic clinopyroxenes are considered accurate, as they are for BHVO-2 which required more substantial interference correction than the samples. In contrast, the ^{87}Sr/^{86}Sr of amphibole, with ^{87}Rb/^{86}Sr of 0.19, may be slightly underestimated by one in the fourth decimal, based on the corrected ^{87}Sr/^{86}Sr for BCR-2G with ^{87}Rb/^{86}Sr of 0.39, which is inconsequential for the conclusions reached in this study. Results for samples both from Wum and from Befang, and for reference materials measured as unknowns, are reported in Electronic Supplementary Material 4.

Electron backscatter diffraction

Thin section preparation for Electron Backscatter Diffraction (EBSD) analyses required mechanic-chemical polishing using a Vibromet. This 1 h15 polish with a colloidal silica suspension (pH 10) removes mechanically-induced surface damage. A JEOL 7100 electron microscope equipped with an EBSD camera HKL Advanced Nordlys Nano from Oxford Instruments, was used at the Microcharacterization Centre Raimond Castaing, Paul Sabatier University, Toulouse, France. The microscope working conditions include an acceleration voltage of 20 kV, a probe current of 16 nA, a stage tilt of 70° and a working distance of 16 mm. Automatic indexing was performed using AZTec software (version 3.5) from Oxford Instruments, with a step size of 20 or 35 μm.

The Channel 5 package was used to perform a standard noise reduction and to extrapolate missing data with at least 8, 7, 6 identical neighbors. Measurements with a mean angular deviation (MAD) greater than 1.3 were removed, and grains were then calculated by imposing an orientation difference smaller than 10° for any two neighboring measurements belonging to the same grain. Grains with a surface smaller than 10 pixels were removed to avoid bias caused by potential indexing error. The maps were compared with band contrast maps to ensure that the treatment did not compromise the data. Resulting EBSD data were then processed in MATLAB using the MTex toolbox (Bachmann *et al.,* 2010, 2011). A lineation has been defined in the xenoliths, using clinopyroxene and orthopyroxene [001] axes, which are parallel and olivine [010] axes perpendicular to clinopyroxene and orthopyroxene [001] axes defining the pole to the foliation plane. For an easy comparison between the xenoliths, the pole figures
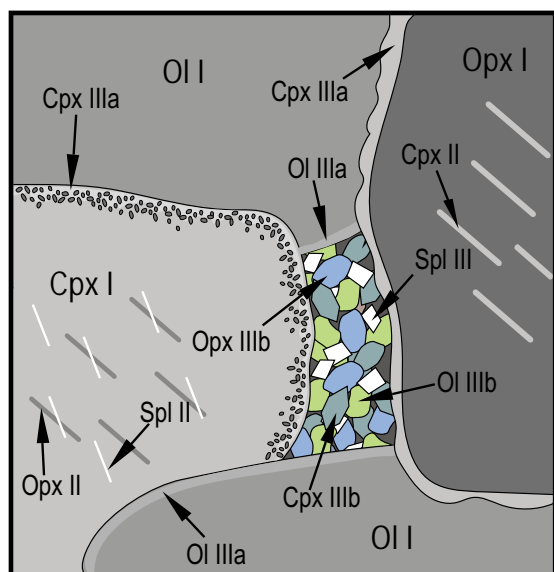
Fig. 2. Illustration of various mineral generations, denoted with Roman numbering of silicate phases and spinel (Ol, olivine; Opx, orthopyroxene, Cpx – clinopyroxene, Spl – spinel) in an exemplary mantle peridotite, showing primary discrete grains, exsolution lamellae and rims/overgrowths, including spongy clinopyroxene rims (analogous to Tedonkenfack et al., 2021).

Fig. 3. Systematic position of xenoliths from Wum in the IUGS classification diagram for ultramafic rocks. Ol, olivine; Opx, orthopyroxene; Cpx, clinopyroxene; D, dunite; O, orthopyroxenite; C, clinopyroxenite.

have been oriented with the lineation sub-parallel to X within the defined foliation plane XY. The multiple uniform density (mud) and the J-index, which is the measure of fabric strength (Bunge, 1982), are reported.

Terminology

The minerals are grouped using an approach similar to that applied in prior papers (Matusiak-Małek et al., 2014; Tedonkenfack et al., 2021). The primary phases are denoted as 'I' (olivine I, orthopyroxene I, etc.), the intergrowths (usually lamellar) in phases I are denoted as 'II', and the minerals occurring in fine-grained interstitial aggregates, as small individual interstitial grains or as margins on primary grains are denoted as 'III' (Fig. 2). To describe rock textures, we use the terminology of Mercier & Nicolas (1975); in some instances, it is coupled with textural terms used in metamorphic petrology to describe rock fabric.

For amphibole, we used the IMA-recommended classification (Hawthorne et al., 2012), with structural formulae calculated by the spreadsheet of Li et al. (2020). Please note that structural formulae in the Electronic Supplementary Material 1 are calculated on $O^{2-} = 23$.

Forsterite content in olivine (Fo) is calculated as atomic $100*Mg/(Mg + Fe + Mn)$ per formula unit. Spinel compositions are based on three cations, with Fe^{3+} and Fe^{2+} calculated by charge balance (Deer et al., 1993). The Cr-number (Cr#) denotes the atomic ratio of $Cr/(Cr + Al)$, and Mg-number (Mg#) denotes atomic $Mg/(Mg + Fe^{tot.})$ in the following.

PETROGRAPHY AND MINERAL CHEMISTRY
Petrography

The xenoliths from Wum are from 5 to 12 cm across in the longest dimension, rounded to subangular. Some of them are friable. The studied suite of xenoliths comprises 14 lherzolites, 2 websterites and 3 olivine websterites, according to the IUGS classification (Fig. 3).
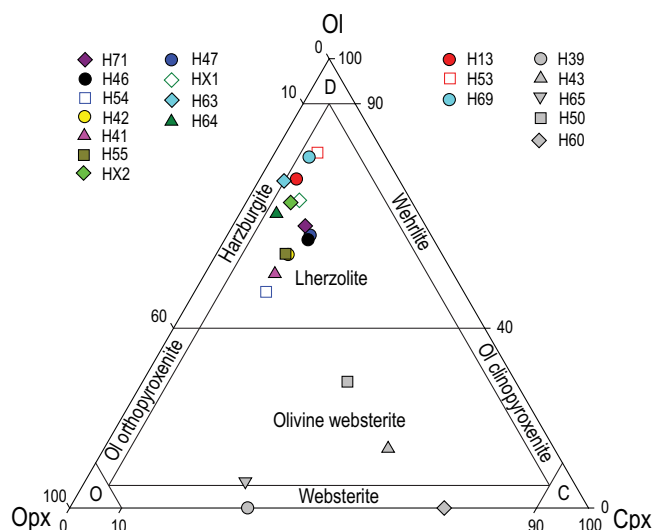
Lherzolites

Lherzolites are porphyroclastic (Fig. 4a) or serial-mosaic (Fig. 4b) to equigranular (Fig. 4c). Weak foliation, defined by streaks of spinel and/or by grain size variation, is visible in some of them (Fig. 4a, b). In porphyroclastic and serial-mosaic rocks, pyroxenes (typically orthopyroxene) form the largest grains up to 15 mm in size (see Table 1).

Phase maps show that olivine forms a continuous framework of contacting grains in lherzolites containing >58 vol.% of this mineral. Pyroxenes and spinel occur as isolated grains and/or aggregates in that framework (Fig. 4d). The olivine framework is locally discontinuous in lherzolites containing less than 55 vol.% of this mineral (H41, H42, H54, H55; cf. Fig. 4a).

The CPO study of lherzolites H71, H46, H42, H47, HX1, H64, H53 and H69 shows similar, well defined olivine patterns with point concentrations on (100) axes parallel to X (supposed lineation) and (010) axes parallel to Z (Fig. 5). The J-index varies between 2.62 and 4.52 except lherzolite H69 showing a J-index of 1.69 (Fig. 5). In lherzolites H47 and H64, the point concentration is stronger on (100) axes whereas in other lherzolites the point concentration is stronger on (010) axes. In most lherzolites, orthopyroxene CPO shows (001) axes forming a point concentration at low angle to olivine (100) axes and to X (Fig. 5). In samples H42 and H46, orthopyroxene and clinopyroxene CPO display similar patterns with a point concentration on (001) axes sub-parallel to Y (at 90° to the lineation), and a point concentration on (010) axes parallel to Z. In a few samples (H47, HX1, and H69), the orthopyroxene (100) or (010) axes form a weak point concentration parallel to Z. In all samples clinopyroxene (001) axes are parallel to X and to orthopyroxene (001) ones, while (010) axes are usually parallel to Z (Fig. 5).

Lherzolite H69 contains significant amounts of amphibole (3.9 vol.%), occurring as interstitial grains or aggregates around spinel, which are texturally later than the olivine-pyroxene fabric (Fig. 4e). Part of the aggregates has asymmetric shapes, and the section is interpreted to show the S-C structure indicative of simple shear (Fig. 4e). Lherzolite H71 contains subordinate amphibole (1.0 vol.%) which is dispersed in incipiently mylonitized groundmass. In both samples, the grains of amphibole do not display internal deformation.
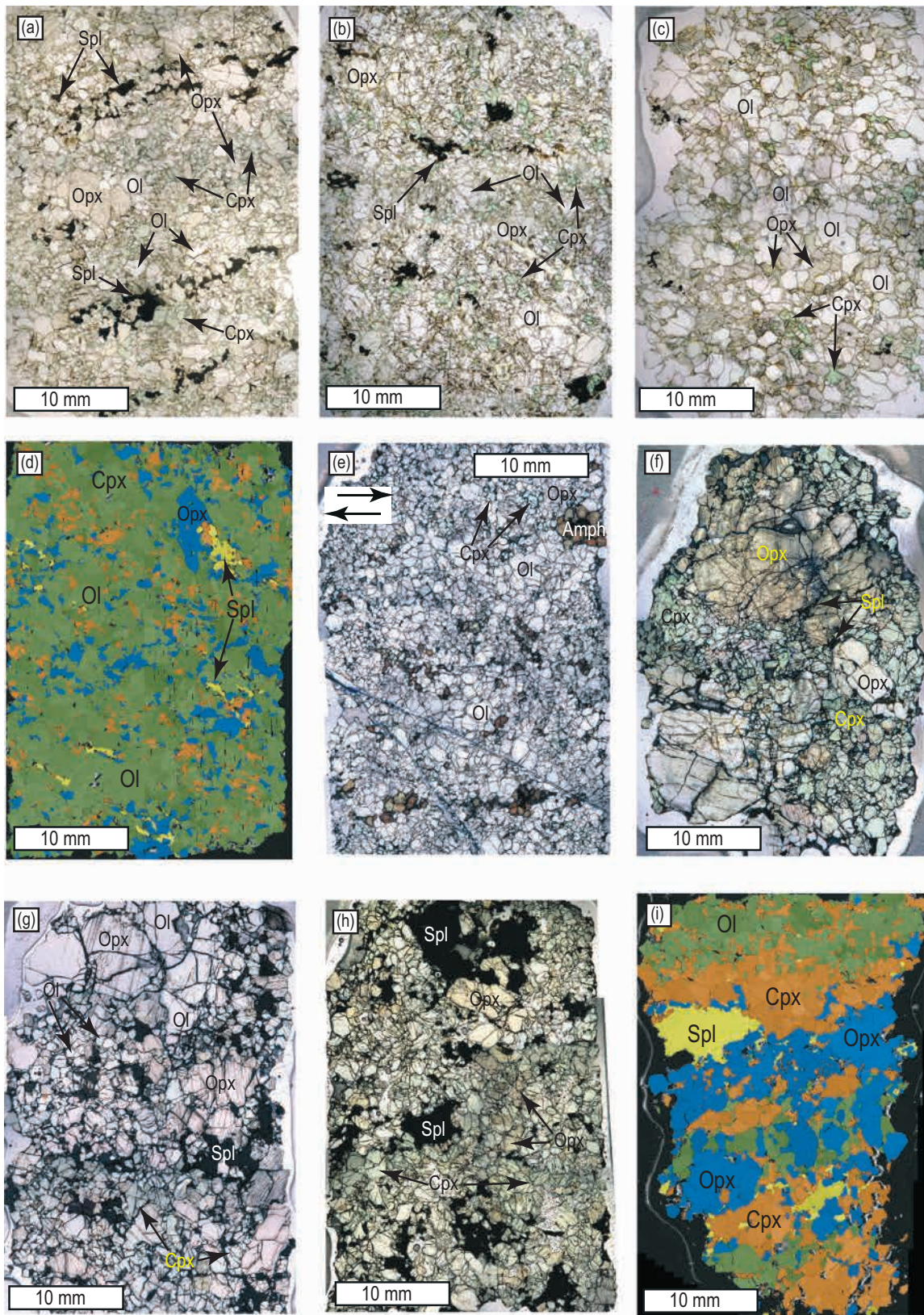
Fig. 4. Textural variation of lherzolites and websterites from Wum. Ol, olivine; Opx, orthopyroxene; Cpx, clinopyroxene; Sp, spinel; Amph, amphibole. (a) Lherzolite H42. Porphyroclasts of orthopyroxene and foliation defined by streaks of spinel and grain size variation. Optical image, plane-polarized light (PPL); (b) Lherzolite H13. Serial, mosaic texture, which partly may be due to unfavorable section. Optical image, PPL; (c) Lherzolite H64. Equigranular texture. Optical image, PPL; (d) Lherzolite H53. Interstitial location of smaller grains of ortho- and clinopyroxene relative to olivine framework. Phase map. (e) Lherzolite H69. Texturally later amphibole occurring in porphyroclastic matrix. Optical image, PPL. (f) Websterite H39. Large porphyroclast of orthopyroxene in a groundmass of ortho- and clinopyroxene. Optical image, plane-polarized light (PPL); (g) Websterite H65 with large amoeboidal grains of spinel. Optical image, PPL; (h) Websterite H60 with abundant spinel grains. Optical image, PPL. (i) Layered websterite H50. Phase map. In the PPL images olivine is white, orthopyroxene creamy, clinopyroxene green and spinel is black.
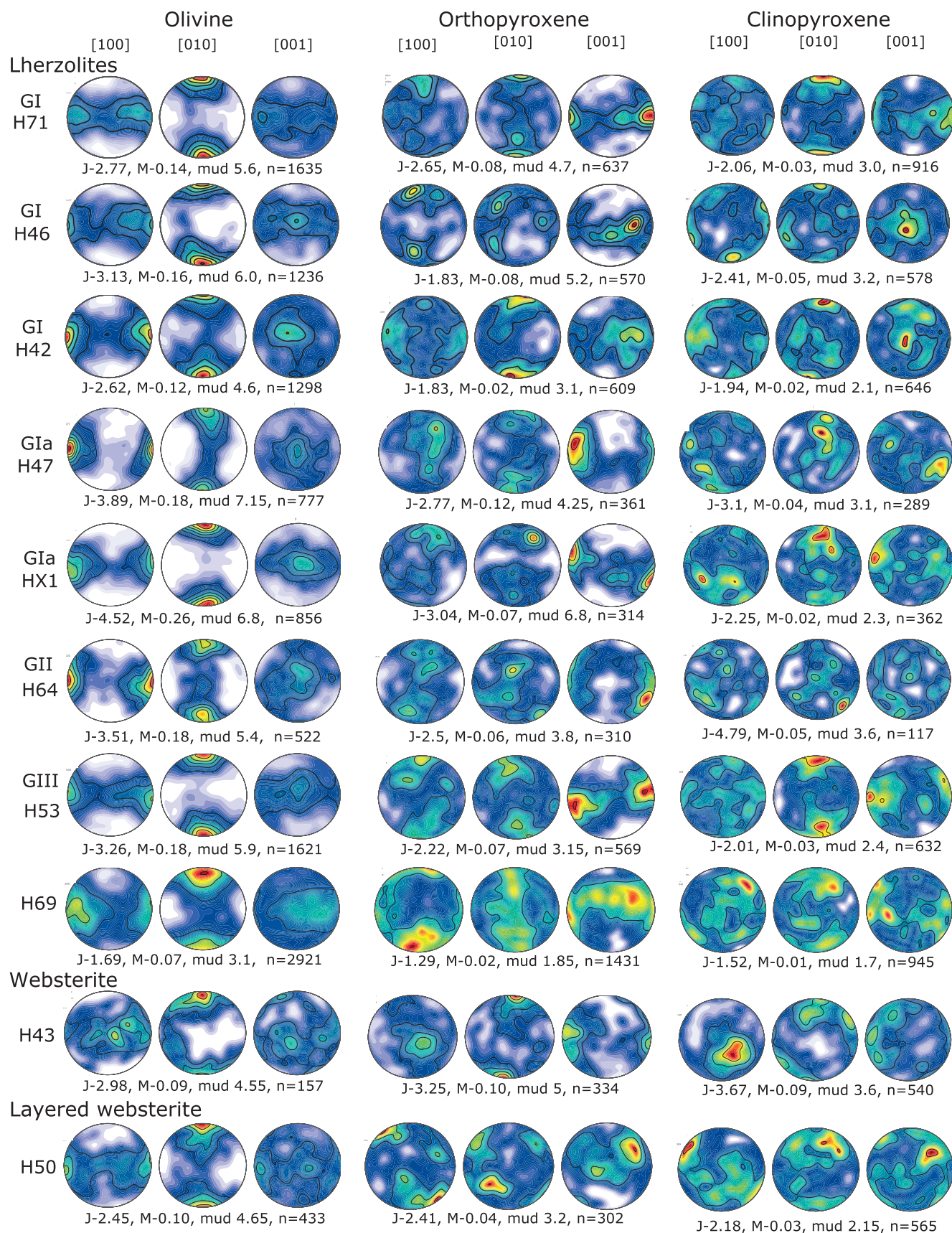
Fig. 5. Crystallographic-preferred orientations (CPOs) of olivine, orthopyroxene and clinopyroxene from Wum xenoliths. Pole figures are lower-hemisphere, equal-area stereographic projection; n is the number of grains and the pole figures represent one point per grain. For all pole figures, contours have been plotted at 0.5 multiples of the uniform distribution (mud). The strength of the CPO was estimated using the J-index (Bunge, 1982).

Websterites

Three of the websterites (H43, H39 and H65) consist of granular pyroxene groundmass in which the porphyroclasts of ortho- or clinopyroxene 10–15 mm across occur (Fig. 4f). The websterite H43 contains a large lamellar clinopyroxene porphyroclast with bent lamellae (Electronic Supplementary Material 5). Websterite H65 contains olivine streaks in addition to pyroxenes and spinel. Its characteristic feature is the occurrence of large amoeboidal to interstitial grains of spinel (Fig. 4g). Websterite H60 is clinopyroxene-rich and contains large spinel grains (Fig. 4h). In this rock the porphyroclasts of orthopyroxene are smaller than in the other websterites, and are associated with spinel grains of similar size. The porphyroclasts occur in the clinopyroxene groundmass in which orthopyroxene is dispersed.

The CPO of websterite H43 is characterized by olivine crystallographic axes showing a concentration of (010) axes parallel to Z, while other axes are scattered in a girdle within the foliation (XY plane) (Fig. 5). Orthopyroxene shows a concentration of (001) axes parallel to X and (010) axes parallel to Z, with a J-index of 3.25. Despite the high proportion of clinopyroxene (54%), it does not display the expected CPO with a point concentration of (001) parallel to Z, but shows the stronger concentration on (100) axes sub-parallel to Y. This sample contains a deformed centimetric clinopyroxene porphyroclast with orthopyroxene lamellae, whose CPO patterns are similar and are also similar to those of the groundmass pyroxene grains (Electronic Supplementary Material 5, Fig. 5).

Xenolith H50 has the composition of olivine websterite (Fig. 3) and consists of millimeter-thick layers dominated by orthopyroxene, clinopyroxene or olivine (Fig. 4i). It displays an olivine CPO similar to those observed in some of the lherzolites (Fig. 5). It is characterized by a strong point concentration on (010) axes parallel to Z, and a weak point concentration on (100) axes parallel to X associated with a weak girdle. In this websterite, orthopyroxene and clinopyroxene (001) axes form a point concentration at slight angle to X and are parallel, and (100) axes are parallel at a slight angle to Z.

Mineral chemistry and $^{87}Sr/^{86}Sr$ of lherzolites

Major and trace element characteristics of minerals allows definition of 'groups' of lherzolites (Table 2). Two of these correspond to the groups defined in the Befang xenolith suite on the basis of REE-patterns in clinopyroxene (Group I – LREE depleted, Group II – LREE enriched; Tedonkenfack et al., 2021). The amphibole-bearing lherzolite H69 cannot be included into any of these groups and is described individually.

Group I

This Group comprises lherzolites H71, H46, H54, H42 with olivine Fo 89.0–89.6 containing from 0.36 to 0.42 wt.% NiO (Fig. 6a) and from <220 to 560 μg/g Ca. These lherzolites have similar Al content in orthopyroxene (0.16–0.19 atoms pfu, Fig. 7) and clinopyroxene (0.27–0.31 atoms pfu, Fig. 7) and contain aluminous spinel (Cr# 0.08–0.10; Fig. 8a). The REE patterns of clinopyroxene (Fig. 9) are practically identical, LREE-depleted (Ce_N/Yb_N of 0.28–0.35; Fig. 10). The $^{87}Sr/^{86}Sr$ ratio in clinopyroxene varies from 0.7017 to 0.7020 (Fig. 10). The lherzolite H71 contains subordinate amphibole (1 vol.%), which texturally is a late addition to the rock. Its REE-pattern is identical to that of clinopyroxene. The lherzolite H46 has traces of amphibole (0.1 vol.%), also a late addition to the rock.

Very similar are lherzolites H41, H55, HX2, HX1 and H47 (olivine Fo 88.8–90.1, NiO 0.34–0.43 wt.%, <220 to 760 μg/g Ca, orthopyroxene 0.17–1.19 atoms Al pfu, clinopyroxene 0.27–0.30 atom Al pfu, spinel Cr# 0.08–0.14; Figs. 6, 7, 8,). Clinopyroxene in these lherzolites is less LREE-depleted compared with that of Group I or is mildly LREE-enriched (Fig.), and its $^{87}Sr/^{86}Sr$ ratio varies from 0.7021 to 0.7028 (Fig. 10), thus these rocks were depicted as Group Ia (Table 2).

The trace element patterns of clinopyroxene from both Group I and Group Ia have negative Ti, Pb and Nb-Ta anomalies (Electronic Supplementary Material 6). This group of lherzolites corresponds to the Group I (LREE-depleted) lherzolites of the neighboring Befang xenolith suite (Tedonkenfack et al., 2021).

Group II

Group II corresponds to the Group II (LREE-enriched) lherzolites from the Befang site (Tedonkenfack et al., 2021) and includes lherzolites H63 and H64 with olivine Fo 89.9–90.0, NiO 0.33–043 wt.% (Fig. 6a), which is Ca rich (820–1240 μg/g). Their pyroxenes are Al-poor (orthopyroxene – 0.15, clinopyroxene 0.23 atoms of Al pfu; Fig. 7). The spinel has Cr# 0.29–0.28 (Fig. 8a). The REE patterns of clinopyroxene are LREE-enriched (Fig. 9), the trace element patterns have negative Ti, Pb and Nb-Ta anomalies, but the latter is shallower than that in clinopyroxene of Group I (Electronic Supplementary Material 6). The $^{87}Sr/^{86}Sr$ ratio in clinopyroxene is 0.7033, which is the highest value among the Wum samples (Fig. 10, Table 2).

Group III

This Group consists of olivine-rich (>70 vol.%; Table 1) lherzolites H13 and H53. The olivine is Fo 90.7%, NiO 0.34–0.40 wt.% (Fig. 6a) and is poor in Ca (<210–430 μg/g). It coexists with Al-poor ortho- and clinopyroxene and spinel with Cr# = 0.18 (Figs. 7 and 8).

The REE patterns of clinopyroxene are 'spoon shaped' (Fig. 9), and the trace element patterns are characterized by well-defined negative Nb-Ta and Ti anomalies and positive U and Pb anomalies (Electronic Supplementary Material 6). The $^{87}Sr/^{86}Sr$ ratio in clinopyroxene from H13 is 0.70212 ± 0.00018 (1σ, n = 8), while that from H53 is 0.70206 ± 0.00020 (1σ, n = 5; Fig. 10), and thus indistinguishable within uncertainty.

Lherzolite H69

This lherzolite consists of Mg-rich (Fo 90.3) and is Ca-poor (180–450 μg/g) olivine containing 0.36–0.44 wt.% NiO, Al-poor orthopyroxene (0.13 atoms pfu) and clinopyroxene (0.255 atoms pfu) and spinel of Cr# 0.20 (Table 2, Fig. 6a, 7, 8). It contains significant amounts of pargasitic amphibole (3.9 vol.%). The REE patterns of clinopyroxene and amphibole are identical, flat from Sm to Lu, and enriched in LREE (La, Ce, Pr, Nd) (Fig. 9). The trace element pattern of amphibole is enriched in Rb, Ba, Nb and Ta as well as in Ti relative to that of clinopyroxene (Electronic Supplementary Material 6). The $^{87}Sr/^{86}Sr$ ratio in clinopyroxene is 0.70267 ± 0.00018 (1σ, n = 5), whereas in amphibole it is 0.70299 ± 0.00005 (1σ, n = 9; Fig. 10).

Mineral chemistry of websterites

We classify the porphyroclastic websterites H39, H43 and H65 as Group 'A' (Table 2), because they contain minerals of almost identical chemical composition. Olivine (if present) contains 89.6–89.7% of Fo, 0.36–0.45 wt.% NiO (Fig. 6a) and 590–840 μg/g of Ca (Table 2). Ortho- and clinopyroxene are aluminous (ca. 0.20 and 0.31 atoms of Al pfu, respectively, Fig. 7, Table 2), as is spinel

Table 2: Summary of chemical characteristics and two-pyroxene equilibration temperatures of rocks from the Wum xenolith suite

Group	Sample	Olivine Fo	Olivine NiO (wt.%)	Olivine Ca (µg/g) min–max; AV	Ortho-pyroxene Al (a pfu)	Clino-pyroxene Al (a pfu)	Clino-pyroxene $^{87}Sr/^{86}Sr$ (m)	Clino-pyroxene Ce_N/Yb_N	Spinel Cr#	T (average) °C
I	H71**	89.61	0.39	<220–370; 310	0.160	0.278	0.7018	0.31	0.10	910
I	H46**	89.52	0.38	<220–410; 320	0.167	0.272	0.7017	0.28	0.10	919
I	H54	89.64	0.39	<220–480; 330	0.167	0.273	0.7017	0.28	0.10	929
I	H42	89.01	0.39	240–560; 390	0.185	0.306	0.7020	0.35	0.08	973
Ia	H41	89.41	0.39	460–760; 630	0.181	0.292	0.7021	0.76	0.10	953
Ia	H55	88.77	0.39	300–530; 420	0.188	0.299	0.7023	0.63	0.08	960
Ia	HX2	90.09	0.39	530–730; 650	0.177	0.281	0.7025	0.46	0.13	961
Ia	HX1	89.78	0.40	<220–430; 300	0.169	0.271	0.7025	2.51	0.11	896
Ia	H47	90.11	0.39	590–790; 670	0.170	0.276	0.7028	1.06/1.38***	0.14	981
II	H63	89.89	0.38	820–1120; 970	0.146	0.234	0.7033	5.81	0.29	1149
II	H64	90.04	0.38	820–1240; 990	0.147	0.233	0.7033	4.06	0.28	1064
III	H13	90.72	0.37	<250–410; 300	0.147	0.245	0.7021	0.48	0.18	881
III	H53	90.76	0.37	<220–430; 320	0.148	0.246	0.7021	0.42	0.18	900
III	H69**	90.26	0.39	<180–450; 290	0.132	0.255	0.7027 0.7031**	3.13	0.20	nc
A	H39*	89.49	0.40	490–790; 700	0.209	0.309	0.7019	0.21	0.04	977
A	H43*				0.200	0.305	0.7020	0.21	0.06	nc
A	H65*	89.74	0.42	590–840; 690	0.207	0.307	0.7017	0.27/0.36***	0.04	996
A	H50*	89.62	0.41	590–840; 730	0.202	0.298	0.7019	0.22	0.05	984
B	H60*				0.252	0.351	0.7031	0.62	0.02	nc

* Websterites and layered cumulitic rock H50
** Amphibole-bearing; $^{87}Sr/^{86}Sr$ (m) in amphibole
*** Varying in the scale of petrographic section
Fo, forsterite content; a pfu, atoms per formula unit; nc, not calculated; AV, average
m, measured and normalized to in-house reference MIR-A (Rankenburg, 2002)
N subscript 'N', primitive mantle-normalized (McDonough & Sun, 1995)
Cr# = atomic Cr/(Cr + Al)
T, average of temperatures of orthopyroxene-clinopyroxene equilibration calculated by methods of Brey & Köhler (2000) and Liang et al. (2013), see text for detailed explanation
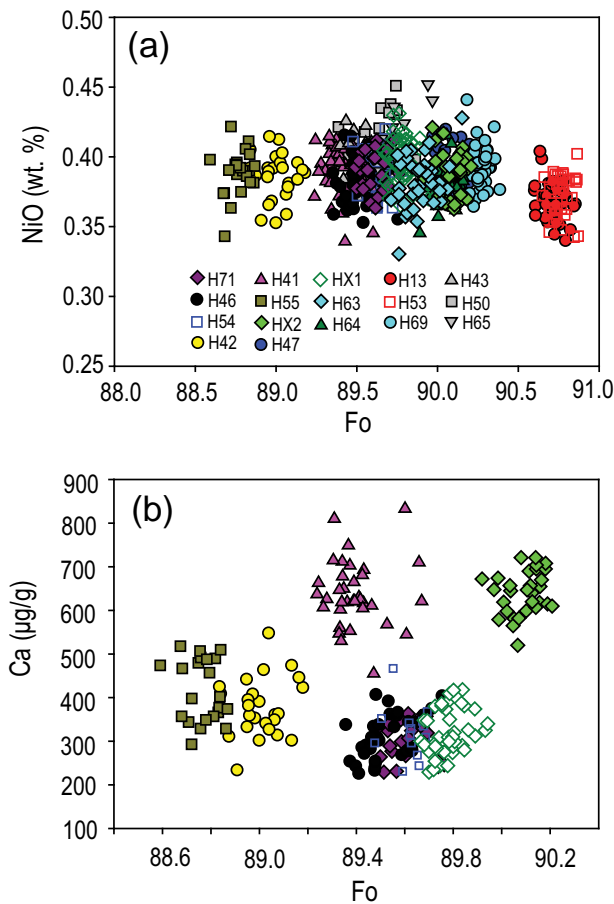
Fig. 6. (a) Olivine compositions in Fo-NiO diagram; (b) Relationships between olivine of I and Ia subgroups in the Fo-Ca diagram. All individual spot analyses per sample are displayed.
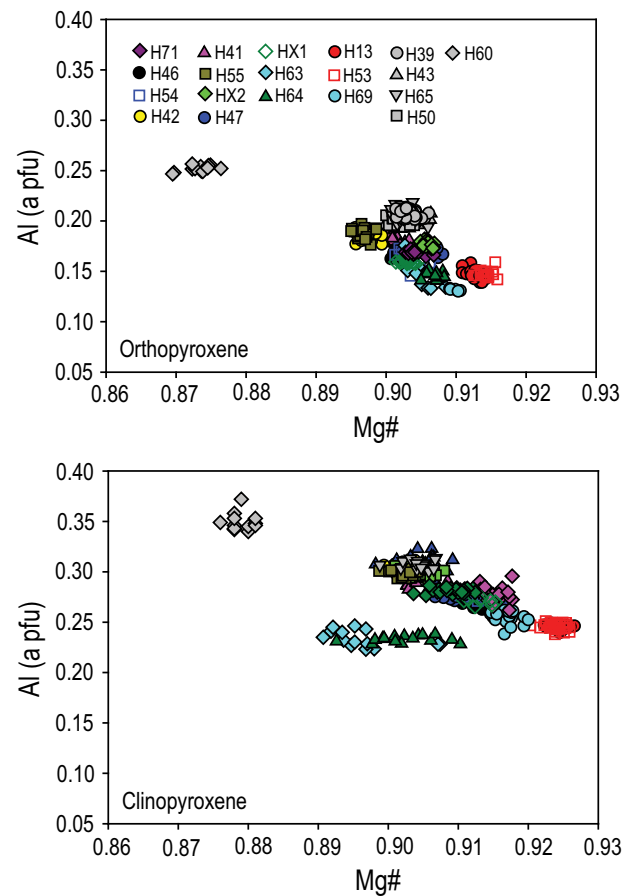

Fig. 7. Ortho- and clinopyroxene compositions in Mg# ($Mg/(Mg + Fe^{total})$) - Al atoms per formula unit (a pfu) diagrams. All individual spot analyses per sample are displayed.

(Cr# 0.04–0.06; Fig. 8a). We include into the 'A' websterites also the layered rock H50, because its minerals are chemically identical to those occurring in other rocks of this Group (Table 2, Figs. 6, 7, 8, 9).

Clinopyroxenes from 'A' websterites have identical REE patterns, which are mildly depleted in LREE relative to HREE (Fig. 9). Olivine websterite H65 contains two populations of clinopyroxene grains, the patterns of which differ slightly by LREE enrichment, and both are LREE-richer than the clinopyroxene patterns of other rocks (Fig. 9). The $^{87}Sr/^{86}Sr$ ratios in clinopyroxene from three studied rocks are identical within uncertainty (H39 and H50– 0.7019, H43–0.7020; Fig. 10, Table 2).

Websterite H60

The clinopyroxene-rich websterite H60 contains aluminous ortho- and clinopyroxene (ca. 0.25 and 0.35 atoms of Al pfu, Fig. 7, Table 2) and extremely Cr-poor spinel (Cr# 0.02; Fig. 8, Table 2). The clinopyroxene REE pattern is depleted in HREE-MREE relative to those of Group 'A' websterites, and mimics them in the LREE except that it has a well-defined positive Eu anomaly (Fig. 9). The trace element pattern has positive Sr anomaly (Electronic Supplementary Material 6). The $^{87}Sr/^{86}Sr$ ratio of clinopyroxene is 0.7031 (Fig. 10, Table 2). This websterite is classified as Group 'B' in Table 2.

Sr isotopic composition of clinopyroxene from the Befang xenoliths

In order to bring the Befang data-set to the same level as that for Wum xenoliths, we obtained $^{87}Sr/^{86}Sr$ ratios for clinopyroxene. They are presented in Table 3, which comprises the set of data on mineral chemistry and temperatures analogous to that which is given for Wum xenoliths in Table 2.

Tedonkenfack *et al.* (2021) defined two groups of lherzolites in the Befang xenolith suite. Group I comprises rocks containing LREE-depleted clinopyroxene which post-dates the major deformation. The $^{87}Sr/^{86}Sr$ ratio of clinopyroxene in this Group varies between 0.7018 and 0.7025. Group II are lherzolites with LREE-enriched clinopyroxene, which shows the same deformation history as olivine and orthopyroxene. Clinopyroxene in this Group has $^{87}Sr/^{86}Sr$ ratios of 0.7024–0.7028, i.e. higher than in Group I. The single harzburgite, which was interpreted to be the protolith for lherzolites, has $^{87}Sr/^{86}Sr$ of 0.7030. The websterite BFA13, which was shown to be deposited from melts analogous to CVL lavas (Tedonkenfack *et al.,* 2021), contains clinopyroxene with a $^{87}Sr/^{86}Sr$ ratio of 0.7034, and also the highest $^{87}Rb/^{86}Sr$ (0.026).

Sulfides in xenoliths from Wum and Befang

In both the Wum and the Befang suites, sulfides occur as subordinate phases enclosed in ortho- or clinopyroxene, rarely in olivine. No significant differences in sulfide textural characteristics occur,
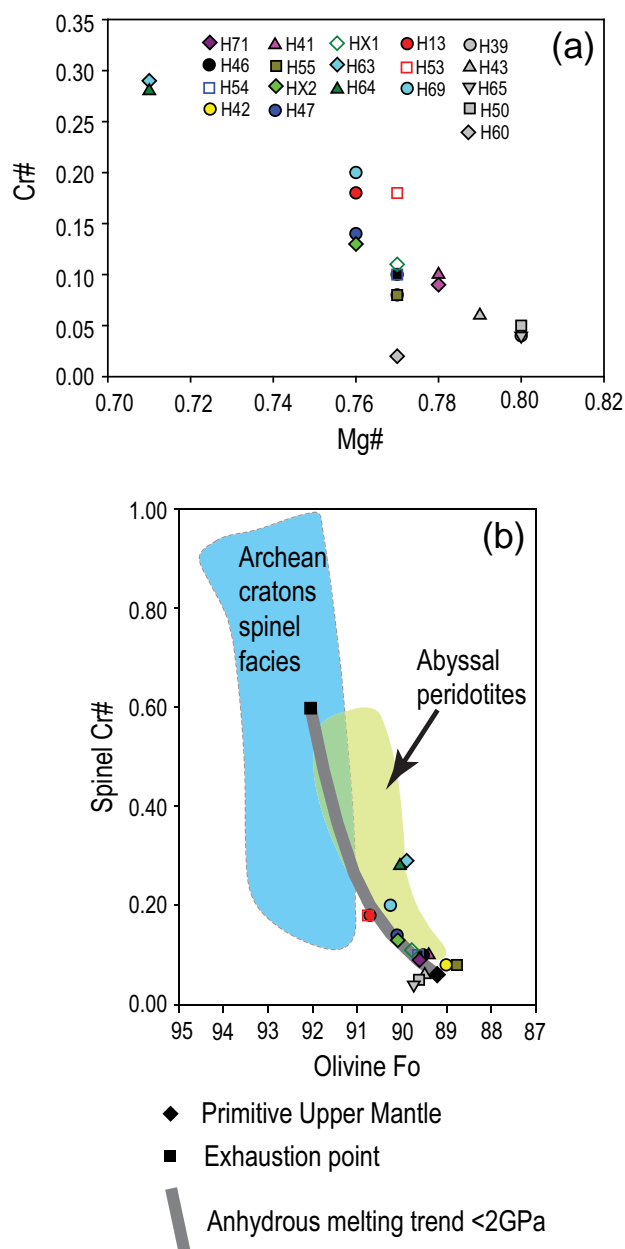
Fig. 8. Average spinel compositions per sample in (a) Mg# (Mg/(Mg + Fe^{total})) - Cr# (Cr/(Cr + Al)) diagram and (b) Cr# - average forsterite content in olivine per sample The fields of Archean and abyssal peridotites, melting trend and exhaustion point and PUM (Primitive Upper Mantle) after the compilation of Scott *et al.* (2019).

between peridotites from Befang and Wum or between different groups of peridotites and pyroxenites defined in this study and in the study of Tedonkenfack *et al.* (2021). Sulfide grains usually form assemblages composed of pyrrhotite (Po), pentlandite (Pn), chalcopyrite (Ccp) and (in very rare cases) cubanite (Cb). These assemblages typically occur as massive Po grains with exsolution lamellae of Pn or as massive crystals separating Po from Ccp. The latter occurs on the rims of sulfide grains or penetrates through entire grains. Cubanite is present only in larger (>100 μm in diameter) sulfide grains as irregular-shaped exsolutions in Ccp.

Sulfides occur in 8 of 14 samples of lherzolites and in 4 of 5 samples of websterites in Wum (Electronic Supplementary Material 9). Sulfides in lherzolites are represented by 13 grains with

sizes varying from 5 to 149 μm (32 μm on average) and modal composition of Po$_{40–65}$Pn$_{0–45}$Ccp$_{9–46}$ (Po$_{49}$Pn$_{31}$Ccp$_{20}$ on average). Sulfides from websterites are represented by 31 grains with sizes varying from 6 to 80 μm (22 μm on average) and modal composition of Po$_{24–99}$Pn$_{1–47}$Ccp$_{0–32}$ (Po$_{45}$Pn$_{32}$Ccp$_{23}$ on average).

Sulfides occur in 7 of 9 Group I xenoliths and in 3 of 5 samples from Group II peridotites from Befang, whereas in websterite BFA13 and harzburgite BFA24 they are absent (Electronic Supplementary Material 9). Sulfides from Group I are represented by 27 grains with sizes varying from 4 to 250 μm (57 μm on average) and modal composition of Po$_{27–100}$Pn$_{0–28}$Ccp$_{0–45}$ (Po$_{59}$Pn$_{22}$Ccp$_{19}$ on average). Sulfides from Group II are represented by 11 grains with sizes varying from 4 to 29 μm (17 μm on average) and modal composition of Po$_{64–81}$Pn$_{8–11}$Ccp$_{10–26}$ (Po$_{73}$Pn$_9$Ccp$_{18}$ on average).

Group I peridotites from Befang and websterites from Wum are characterized by the highest number of sulfide grains from this xenolith suite. Maximum and average sizes of sulfides are variable. Two anomalously-large-sized grains were found in lherzolite BFA16 (250 μm-sized grain; Befang Group I) and in lherzolite H54 (149 μm-sized grain; Wum Group I). These two grains consist of Ccp with Cb exsolutions.

Thermometry

To estimate the temperatures at which the studied rocks resided before entrainment in the erupting lavas, we used geothermometers based on ortho- and clinopyroxene pairs. We applied the classical two-pyroxene geothermometer of Brey & Köhler (1990) and the REE-partitioning geothermometer of Liang *et al.* (2013). The results are reported in Table 2 and the details of calculations are summarized in Electronic Supplementary Material 8.

The two-pyroxene geothermometer of Brey & Köhler (1990) is based on exchange of Mg, Fe, Ca and Na between coexisting ortho- and clinopyroxene. This geothermometer refers to the four-phase lherzolite, i.e. the system which is saturated in olivine, ortho- and clinopyroxene and spinel or garnet. For calculations, we used analyses of points located in the neighboring orthopyroxene I and clinopyroxene I grains. The majority of points were located well inside the grains, but we used also analyses located within a few tenths of microns from the margins. We used 6–25 pairs of points. The limiting factor in some sections was the number of ortho- and/or clinopyroxene grains. In one of the sections (HX1) the Na content in orthopyroxene was below the detection limit of the microprobe, and we used a Na content equal to 0. The temperature calculation results are identical when the Na content at the detection limit (300 μg/g, which equals to 0.04 wt.% of Na$_2$O) is used. For more details on the temperature calculations in this section see Electronic Supplementary Material 8.

The ortho- and clinopyroxene are homogeneous in terms of both major- and trace element distribution in most of the studied rocks (cf. Electronic Supplementary Materials 2 and 3), which enables the application of geothermometers based on element partitioning between these two phases. The exception is lherzolite H63, which is discussed in detail in Electronic Supplementary Material 8.

In most of the studied rocks the results for various pairs per sample differ by <33°C (Electronic Supplementary Material 8). Because the two-pyroxene geothermometer reproduces equilibration temperatures within 30°C (Brey & Köhler, 1990), we believe that these results indicate equilibrium between ortho- and clinopyroxene. In some samples the difference is greater (H54–50, H47–41, H42–37°C) reflecting individual pairs of points yielding results significantly different from the majority. We consider
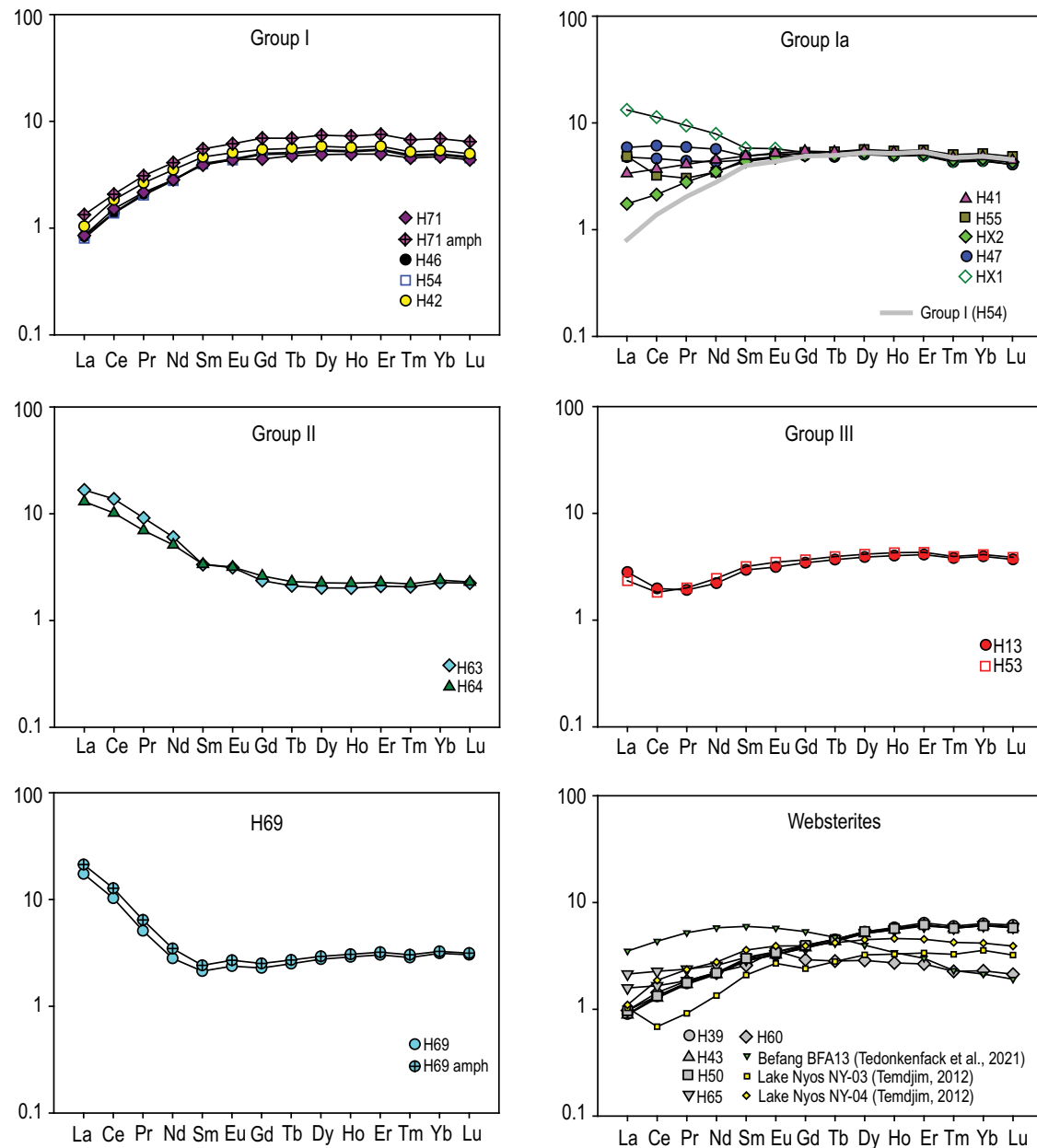
Fig. 9. PM-normalized (McDonough & Sun, 1995) REE patterns of clinopyroxene from the Wum xenoliths shown according to grouping (see text for details); also shown is amphibole pattern for sample H69. The patterns of clinopyroxene from websterites from Befang (Tedonkenfack *et al.*, 2021) and Lake Nyos (Temdjim, 2012) are shown for comparison in websterite panel.

also those samples as equilibrated. Six pairs of points located at the margins of neighboring pyroxenes in lherzolite H47 yield temperatures 1033–1098°C, which we consider as the effect of a thermal event which affected the rock but was too short-lived to re-equilibrate the compositions of entire grains.

Lherzolite H71 contains subordinate amphibole, which is texturally late. It seems to have no effect on the composition of pyroxenes, therefore the temperatures were calculated as in the amphibole-free rocks. Lherzolite H69 contains more amphibole. Although it is also texturally late, the composition of pyroxenes in this rock is different compared with other lherzolites. Therefore, we assume that amphibole formation affected the composition of pyroxenes and exclude this rock from pyroxene thermometry.

The orthopyroxene from layered websterite H50 contains lamellae of clinopyroxene, which yield lamella-host temperatures

of ca. 1125°C, significantly higher than the temperature of equilibration between discrete grains (ca. 989°C).

The spreadsheet of Liang *et al.* (2013, online supplementary material) includes temperature calculations according to the algorithm of Brey & Köhler (1990). As an input composition we used averaged composition of ortho- and clinopyroxene I in each sample. The temperatures calculated this way differ by only a few degrees Celsius from averages of individual grain pairs (Electronic Supplementary Material 8).

Averaged contents of REEs in grains of ortho- and clinopyroxene are an input for the REE geothermometer of Liang *et al.* (2013). The variation in LREE contents in analyses of orthopyroxene is greater than that of MREE-HREE due to the mass spectrometer working at the limits of detection, as outlined above (see *LA-ICP-MS analyses*). To avoid these effects, we used the elements the
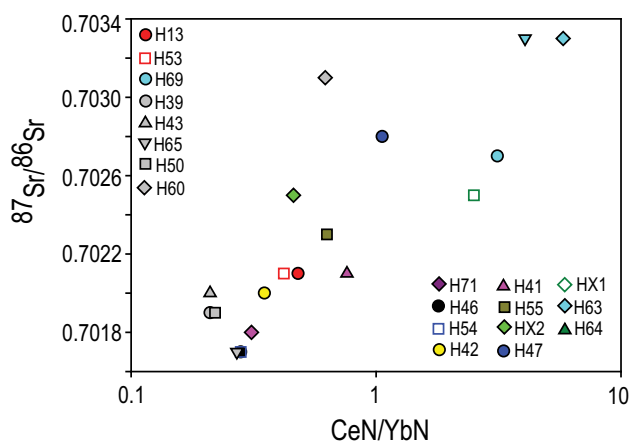
Fig. 10. Relationship between CeN/YbN (where N denotes normalization to Primitive Mantle of McDonough & Sun, 1995) and $^{87}Sr/^{86}Sr$ ratios in clinopyroxene from the Wum xenoliths.

averages of which have relative standard deviation (RSD) ≤ 15% except 2 rocks where elements with RSD 17 and 20% had to be used (Electronic Supplementary Material 8). In most rocks the difference between the REE-based temperature and that based on major elements was smaller than 12°C. The exceptions are lherzolites H41 (ΔT 24°C), H47 (ΔT 18°C), H63 (ΔT 58°C) and H64 (ΔT 39°C, see data in Electronic Supplementary Material 8).

DISCUSSION
Thermal evolution of the lithosphere

Most of the xenoliths from Wum and Befang show consistent temperatures of pyroxene equilibration varying between 900 and 1000°C. The temperatures calculated based on major and trace element exchange (Brey & Köhler, 1990; Liang et al., 2013, Tables 2 and 3) are identical within the geothermometers' uncertainties (~ 30°C). This suggests that after the pyroxenes were formed, their host peridotites reached thermal equilibrium that was not disturbed prior to entrainment. Mantle residence temperatures were preserved in xenoliths when they were recently (< 1 Ma) entrained into the erupting lavas and brought to the surface. This means that possible recent short-term advective heating of mantle during CVL volcanism is not recorded in the samples from Wum and Befang and therefore that the lithospheric mantle profile was under steady-state thermal condition when sampled by the lavas.

The insignificant effect of recent Oku volcanism on the underlying mantle lithosphere is also indicated by the study of Asaah et al. (2021), which shows that most (>85%) of the Oku Volcanic Group lavas, which erupted during last 12 Ma, come from asthenospheric sources and are not contaminated by lithospheric mantle. This coincides with our observation that no record of reactive percolation of CVL lavas occurs in the xenoliths from Befang (Tedonkenfack et al., 2021; 16 xenoliths studied in detail) and Wum (this study; 19 xenoliths studied in detail). As will be discussed in more detail below, in both xenolith suites we have found only one xenolith of websterite with trace element and $^{87}Sr/^{86}Sr$ characteristics indicating an origin by crystal accumulation from lavas identical to those occurring in the Oku Volcanic Group (BFA13; Tedonkenfack et al., 2021 and this study).

The steady thermal state of mantle lithosphere at the time of xenolith entrainment allows the independently constrained regional geotherm to collocate the xenoliths in the lithosphere

column without a prior knowledge of their pressures of equilibration. One approximation of the LAB depth is the intersection of the mantle adiabat (1300°C potential temperature) with the steady-state geotherm, here taken to be the 60 mW/m² geotherm of Hasterok & Chapman, which crosses the adiabat at a depth of 90 km (Fig. 11), as independently constrained from seismic observations (Goussi Ngalamo et al., 2018, see *Geological Context*).

At the steady-state thermal conditions recorded by the xenoliths, a monosulfide is expect to be stable (Naldrett et al., 1967; Naldrett & Kullerud, 1967; Kullerud et al., 1969), which decomposes into a low-temperature assemblage (Craig & Kullerud, 1969; Craig, 1973; Lorand, 1989; Makovicky & Karup-Møller, 1995; Alard et al., 2000; Lorand & Grégoire, 2006). As such, the formation of pentlandite lamellar exsolutions in pyrrhotite and cubanite exsolutions in chalcopyrite took place at temperatures lower than those occurring in the mantle: 650–350°C (Kullerud & Yoder, 1959; Kullerud, 1963; Kelly & Vaughan, 1983; Kaneda et al., 1986) and at around 210°C (Lusk & Bray, 2002), respectively.

The nature of websterites from the Oku mantle section

Websterite xenoliths are significant in Wum (5 of 19 samples) and scarce in Befang (1 of 16 samples; Tedonkenfack et al., 2021). Four of those from Wum (H39, H43, H65 and H50) are chemically identical and are classified as Group 'A', whereas one websterite from Wum (H60) is different and is classified as Group 'B' (Table 2). The websterite H13 from Befang is depicted as Group 'C' in Table 3 and in the following.

Websterites of group 'A'

The relative abundance of Group 'A' websterite xenoliths suggests that they are common in the lithospheric mantle beneath the Oku Volcanic Group. The websterites classified as Group 'A' have very similar mineral compositions (Figs. 6, 7, 8, 9). Their pyroxenes and spinel are aluminous, clinopyroxene is LREE-depleted and has low, unradiogenic $^{87}Sr/^{86}Sr$ of 0.7020–0.7017 (Fig. 10, Table 2). Olivine, which occurs subordinately in three of them, contains 89.5–89.7% of forsterite and 490–840 μg/g of Ca (Table 2).

Constraints on the 'A' websterites' petrogenesis from petrographic observations and EBSD study. Fine-grained websterite H50 exhibits layering which suggests that it could have originated by crystal precipitation from silicate melt. This is supported by olivine CPO with girdles on (100) and (001) axes and a strong concentration on (010) axes perpendicular to the foliation plane. This kind of CPO has been observed in magmatic cumulates (Holness et al., 2017; Henry et al., 2021) or during deformation in the presence of melt (e.g. Holtzman et al., 2003). Olivine displays a weak point concentration on (100) parallel to X and large crystals show few low-angle boundaries suggesting weak plastic deformation probably related to compaction (Holness et al., 2017). The internal deformation of clino- and orthopyroxene is almost inexistent, and their grains display a point concentration on (001) axes at 45° to X (Fig. 5). This indicates that (1) they crystallized after olivine and (2) their primary CPO was not overprinted by strong plastic deformation.

The other three websterites of Group 'A' are porphyroclastic with porphyroclasts of both clino- and orthopyroxene embedded in a recrystallized matrix (Table 1). The 10–15 mm porphyroclasts in H39 and H43 suggest that their protoliths were coarse-grained before the onset of deformation. A large clinopyroxene porphyroclast with kinked lamellae in H43 documents lamellae unmixing, probably during cooling, followed by deformation (Electronic Supplementary Material 5). The final effect of this deformation was grain-size reduction and recrystallization of the

Table 3: Summary of chemical characteristics and two-pyroxene equilibration temperatures of rocks from the Befang xenolith suite (Tedonkenfack et al., 2021), and this work)

Group[1]	Sample	Olivine Fo	Olivine NiO (wt.%)	Olivine Ca (μg/g)	Orthopyroxene Al (a pfu)	Clinopyroxene Al (a pfu)	Clino-pyroxene $^{87}Sr/^{86}Sr(m)$ [2]	Clino-pyroxene Ce_N/Yb_N	Spinel Cr#	T (average) °C [2]
I	BFA28	89.6	0.39	580–750	0.190	0.281	0.7018	0.17	0.09	987
I	BFA43	89.4	0.38	450–750	0.180	0.291	0.7019	0.71	0.10	nc
I**	BFA3	89.3	0.37	250–400	0.177	0.297	0.7019	0.51	0.11	964
I (Ia)	BFA35	89.8	0.39	450–730	0.181	0.296	0.7022	0.47	0.10	967
I (Ia)	BFAx	89.7	0.37	260–500	0.177	0.292	0.7023	0.33	0.11	969
I (Ia)	BFA17	89.9	0.39	420–650	0.176	0.289	0.7024	0.39	0.09	977
I (Ia)	BFA16	89.1	0.38	280–570	0.188	0.300	0.7025	0.31	0.09	984
I (Ia)	BFA31	89.8	0.38	450–680	0.175	0.284	0.7025	0.47	0.11	992
I (Ia)	BFA7	90.0	0.39	450–690	0.177	0.281	0.7025	0.37	0.11	966
II	BFA23	89.5	0.39	300–490	0.178	0.300	0.7028	1.13	0.09	936
II	BFA33	89.2	0.38	180–400	0.175	0.278	0.7027	2.20	0.11	951
II	BFA29	88.7	0.38	380–530	0.181	0.286	0.7026	0.96/1.43/1.85***	0.09	963
II	BFA36	90.1	0.39	550–750	0.171	0.250	0.7026	1.22/1.82***	0.15	nc
II	BFA42	89.8	0.38	220–420	0.169	0.275	0.7024	0.62	0.11	nc
II	BFA24	90.3	0.39	200–400	0.151	0.244	0.7030	0.45	0.19	937
C	BFA13*	-	-	-	0.154	0.226	0.7034	2.03	-	nc

[1] In parentheses are classifications according to the approach in this study [2] This study
* Websterite
** This sample was included in Group 2 by Tedonkenfack et al. (2021)
*** Varying in the scale of petrographic section
Fo, forsterite content; a pfu, atoms per formula unit; nc, not calculated
m, measured and normalized to in-house reference MIR-A (Rankenburg, 2002)
N, primitive mantle-normalized (McDonough & Sun, 1995)
Cr# = atomic Cr/(Cr + Al)
T, average of temperatures of orthopyroxene-clinopyroxene equilibration calculated by methods of Brey & Köhler (2000) and Liang et al. (2013), see text for detailed explanation
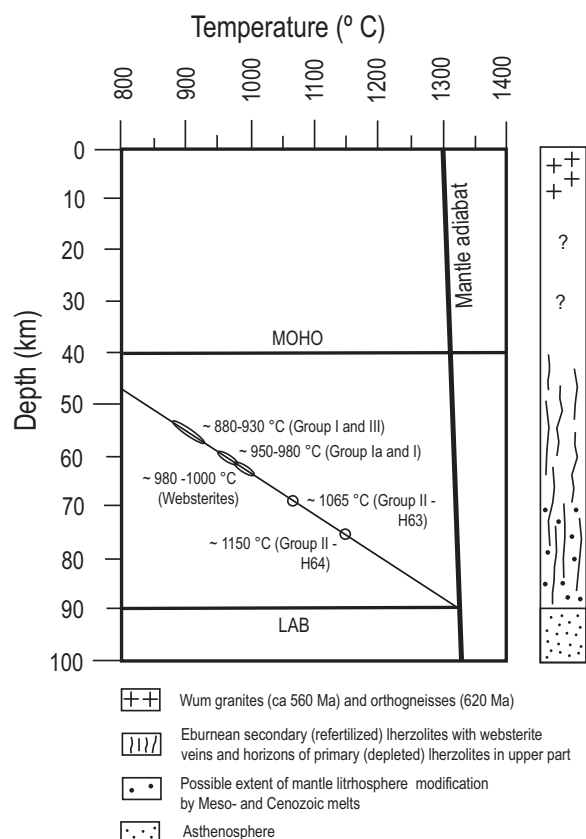
Fig. 11. Position of lherzolites and websterites from Wum as projected onto a 60 mW/m² geotherm (from Hasterok & Chapman, 2011). The depth to the Moho discontinuity and that to LAB constrained by geophysical studies (Goussi Ngalamo *et al.,* 2017, 2018; see text for details). Ages of Wum granitoids are from Li *et al.* (2017).
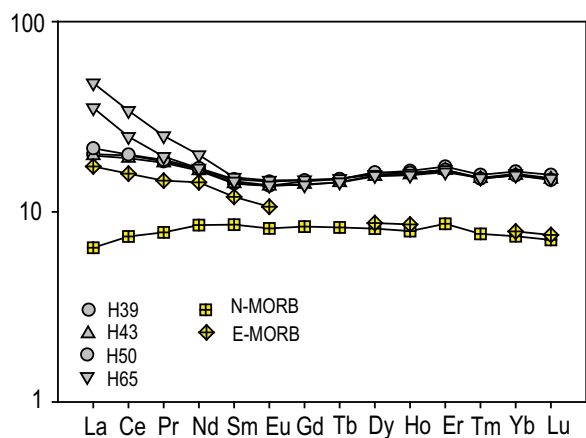

Fig. 12. Hypothetical melts calculated on a basis of clinopyroxene composition from type 'A' websterites compared with average N-MORB (after Gale *et al.,* 2013) and to analysis of E-MORB (Waters *et al.,* 2011, analysis no 2703-1 in their Table 3). PM-normalized (McDonough & Sun, 1995).

newly formed matrix. This resulted in ordering of CPO of olivine and pyroxenes in the matrix and low internal deformation of the clinopyroxene porphyroclast (Fig. 5 and Electronic Supplementary Material 5). The porphyroclast is not completely obliterated by grain size reduction and recrystallization, but most of the lamellar ortho- and clinopyroxene are oriented similarly to matrix grains, and the lamellar structure is partly replaced by a granular one

(Electronic Supplementary Material 5). The chemical composition of pyroxenes shows limited variation and the composition of lamellae in the porphyroclast does not differ from that of matrix grains (Electronic Supplementary Material 1). Because the major element composition of ortho- and clinopyroxene is not equilibrated, temperature calculation by the method of Brey & Köhler (1990) yields results varying between 925 and 1052°C. The contents of trace elements and REE show also variation, especially in orthopyroxene, which probably also is a result of imperfect equilibration (Electronic Supplementary Material 2).

Parental melt of the Group 'A' websterites. In order to constrain the identity of the melt from which the Group A websterites accumulated, the REE patterns of hypothetical melts from which the clinopyroxene crystallized were calculated using measured REE contents in clinopyroxene and diopside-melt partition coefficients of Yao *et al.* (2012) for a DMM source at 1400°C (see Table 4 in Yao *et al.,* 2012). Because the partition coefficients were obtained at supra-solidus conditions, whereas the samples resided at subsolidus conditions, the accuracy of the resulting element abundances in the hypothetical melts may be adversely affected by subsolidus element redistribution (e.g. Lin *et al.,* 2022). This is particularly so for Zr, Nb and HREE, which may be redistributed to clinopyroxene on cooling (Witt-Eickschen & O'Neill, 2005; Sun & Liang, 2014), and likely applies to other trivalent and higher-valence cations. Bearing these caveats in mind, the patterns of the hypothetical equilibrium melts are superficially similar to E-MORB, with respect to the negative slope in the LREE, and clearly dissimilar from the N-MORB, which is depleted in the lightest REE relative to Pprimitive Mantle (Fig. 12). However, E-MORB does not fit the hypothetical melts with respect to MREE-HREE abundances, which are markedly higher.

Websterite H65 shows a distinct change in slope in the LREE part of the pattern of the hypothetical melt in equilibrium with clinopyroxene. This enrichment varies across the thick section (Electronic Supplementary Material 7), and is interpreted to reflect local variation of the LREE concentration of the parent melt due to reactive percolation through peridotite, leading to disequilibrium enrichment of the melt in the more incompatible elements (e.g. Hauri, 1997; Bodinier *et al.,* 2004). That is, apart from possible complications arising from subsolidus trace element redistribution, the premise of full equilibrium with a melt is not fulfilled for sample H65. Reactive melt percolation may also have caused sulfide saturation in the melt via reduction of melt volume (e.g. Wittig *et al.,* 2010), explaining the presence of sulfide in Group A websterites (Electronic Supplementary Material 9).

In contrast to the LREE, the patterns of the less incompatible REE (Sm-Lu) in all hypothetical melts in equilibrium with websteritic clinopyroxene are remarkably similar and flat, and they are higher than in both N-MORB and E-MORB. If this feature is robust, it suggests that the parental melt left a garnet-free (therefore probably shallow spinel-facies) source, which otherwise would have more strongly retained HREE than MREE, imparting a negative slope in the Sm-Lu pattern. Furthermore, it must have formed by lower melt fractions than typical MORB, allowing incompatible elements to be overall more enriched than in MORB. A melt fraction <N-MORB can explain the small, but distinct negative slope in the LREE of the hypothetical melts calculated for websterites other than H60, although the influence of reactive melt percolation cannot be excluded. A melt fraction <N-MORB would be easily rationalized by the presence of a pre-existing continental lid, which impedes decompression melting, whereas this constraint is not given at mid-ocean ridges (e.g. Niu *et al.,* 2011).

Constraints on the 'A' websterites' petrogenesis from $^{87}Sr/^{86}Sr$ ratios in clinopyroxene. The striking feature of Group A websterites is the very low $^{87}Sr/^{86}Sr$ ratio of 0.7020–0.7017 of clinopyroxene. Given their suggested cumulate origin and that clinopyroxene is the main host of incompatible elements in spinel peridotite, the accumulating crystals would have very low Rb/Sr of 0.0015 ($^{87}Rb/^{86}Sr$ of 0.0042), based on clinopyroxene-melt KD Rb/Sr of 0.1 (Adam & Green, 2006) and 1.84 $\mu g/g$ Rb and 128 $\mu g/g$ Sr in average N-MORB (Gale *et al.*, 2013). Such low parent-daughter ratios would cause severely reduced ingrowth of radiogenic ^{87}Sr, which would retain close to initial isotopic compositions. A Primitive Mantle would have had $^{87}Sr/^{86}Sr$ of 0.7017–0.7020 2.0–2.25 Ga ago, calculating back from the modern estimate of $^{87}Sr/^{86}Sr = 0.7045$ and Rb/Sr = 0.0307 (Workman & Hart, 2005), using the decay ^{87}Rb constant of Steiger & Jäger (1977). This Paleoproterozoic age is in perfect agreement with the Lu-Hf and Re-Os isotope ages obtained for CVL xenoliths by Liu *et al.* (2020), testifying to an unsuspected robustness of the Rb-Sr isotope system in parts of the regional lithospheric mantle.

Another possibility is that the websterite parental melt was extracted from a source which itself was subjected to ancient episode of minor melt extraction, that retained some fertility but produced a residuum that was depleted in Rb and evolved at low time-integrated Rb/Sr. The modern average DMM has $^{87}Sr/^{86}Sr$ of 0.7026 compared with 0.7045 for PM, but the DMM reservoir is not homogeneous and contains portions that are more depleted (D-DMM), with present-day $^{87}Sr/^{86}Sr$ of 0.70219 (Workman & Hart, 2005). The $^{87}Sr/^{86}Sr$ of this reservoir would have been lower in the past, depending on the Rb/Sr of this source, and may have generated melts with the unradiogenic Sr and depleted source characteristics that were subsequently inherited by the Group A websterites.

Websterite H60 (group 'B')

The olivine websterite H60 is different from the websterites of Group A. Its pyroxenes and spinel are extremely aluminous and less magnesian (Figs. 7, 8, Table 2), the REE pattern of clinopyroxene is has low HREE/MREE relative to websterites of Group A (Fig. 9) and trace element pattern has well defined positive Eu and Sr anomalies (Electronic Supplementary Material 6). These characteristics suggest that the melt source once contained plagioclase and that the residuum after melting contained garnet, thus the melt source was deeper-seated than that from which Group A websterites formed. Secondary lherzolites metasomatized by melts of similar characteristics occur in the Ronda Massif in Spain (Marchesi *et al.,* 2013). The rock contains large spinel grains (Fig. 4), but no sulfide is present, suggesting that the parental melt did not reach sulfide saturation, in contrast to Group A websterites (Electronic Supplementary Material 9). The $^{87}Sr/^{86}Sr$ ratio of clinopyroxene (0.7031) is distinctly higher than those of clinopyroxenes from Group A websterites, though still lower than PM at 0.7045 (Workman & Hart, 2005). Websterite H60 may document the subduction episode which operated in the upper mantle beneath the Central African Orogenic Belt (CAOB) in its part underlying the CVL. The subducted plate could have been the source of water which enabled the crystallization of amphibole in the Oku lithospheric mantle, discussed further below.

Comparison to websterites from the neighboring localities

Websterite BFA13 from the Befang xenolith suite (Tedonkenfack *et al.,* 2021) is different from those described in this study. It contains neither olivine nor spinel, and pyroxenes are poor in Al, while clinopyroxene is LREE-enriched (Fig. 9). Tedonkenfack *et al.* (2021) indicate that it possibly originated by pyroxene settling from melt similar to recent Oku alkaline lavas, and speculated that similar websterites form veins marking alkaline lava pathways in the Befang lithospheric mantle. The $^{87}Sr/^{86}Sr$ ratio of clinopyroxene (0.7034, Table 3) falls in the range of the Oku volcanic rocks, which vary between 0.70316 and 0.70358 (Asaah *et al.*, 2015), supporting this view.

Two websterites have been described by Temdjim (2012) from the Lake Nyos xenolith suite. Despite the presence of abundant olivine (NY-03: 23 vol.%, NY-04: 31 vol.%), NY-03 is similar, both in terms of major and trace element compositions of minerals, to websterites of Group A from Wum. However, it contains 1 vol.% of amphibole, which is chemically similar to that occurring in lherzolite H71. By analogy with lherzolite H71 (discussed below), we suggest that amphibole crystallized later than the minerals of the host (see *Origin of amphibole in the Oku lithospheric mantle*). Websterite NY-04 consists of minerals which are different from the other websterites described here (olivine Fo 90.8, orthopyroxene Al 0.15–0.17 atoms pfu, clinopyroxene Al 0.26 atoms pfu, spinel Cr# 19.8). Its clinopyroxene is LREE-depleted but its pattern is different from those of other websterites (Fig. 9).

The evolution of the Oku mantle lithosphere
Insights from fabric

Xenolith suites from Wum (this study) and Befang (Tedonkenfack *et al.,* 2021) are dominated by the lherzolites of Group I (Tables 2, 3). Crystal-preferred orientation studies of both suites (this study and Tedonkenfack *et al.,* 2021) shows that lherzolites of Group I consist of an olivine framework having consistent fabric, in which differently oriented grains of spinel and clinopyroxene occur. Orthopyroxene either forms part of the olivine framework (Tedonkenfack *et al.,* 2021) or may be oriented independently of it (lherzolites H42 and H46 from Wum).

These relationships suggest a record of intergranular melt percolation in the peridotite protolith, which enabled crystallization and/or recrystallization of spinel, clinopyroxene and locally orthopyroxene in a solid framework consisting of olivine ± orthopyroxene. Similar fabric relationships were described and analogously interpreted in peridotite xenoliths by Kaczmarek *et al.* (2016); Morales & Tommasi (2011); Puziewicz *et al.* (2020);, Tedonkenfack *et al.* (2021); Tommasi *et al.* (2008) and Zaffarana *et al.* (2014).

The fabric relationships discussed above suggest that the lherzolites of Group I evolved analogously to those occurring in the Lherz massif in the Pyrenées, which originated by reactive infiltration of LREE-depleted MORB-like melt into a harzburgitic protolith, which was LREE-enriched (Le Roux *et al.,* 2007, 2009). The major, trace and Sr isotopic characteristics of various rocks formed during melt infiltration in the Lherz massif correspond to those occurring in the Wum and Befang xenolith suites.

In xenolith-based studies, information on spatial relationships among various lithologies is not available. However, we can use thermal stratigraphy in order to find the relative positions of the xenoliths and to identify those that may have come from the immediate vicinity of refertilized Group I lherzolites. This is justifiable because the geothermometry shows that after the melt-percolation event the mantle lithosphere relaxed thermally, and the temperatures recorded in xenoliths therefore represent the steady-state geotherm (see *Thermal evolution of the lithosphere* above).

The mechanism of intergranular melt percolation

The Oku mantle section may have been affected by intergranular silicate melt percolation, by a mechanism which is analogous to that described in the pioneering studies of J. L. Bodinier and coworkers in the Ronda massif (e.g. Bodinier et al., 2008; Lenoir et al., 2001; Soustelle et al., 2009; van der Wal & Bodinier, 1996; and references therein).

If the rock is below its solidus, the grain interstices are clogged and do not offer pathways for melt percolation. When the rock starts to melt, the volume of solid grains is reduced and eventually an interconnected network of interstitial melt is formed, the geometry of which depends on its volume and wetting characteristics (see e.g. Zhu et al. 2011). The ratio of melt to solid is dictated by rock composition and degree of departure from the solidus conditions in P–T space (Fig. 13). This melt can move ('percolate') if the local conditions generate the pressure gradient necessary to force melt migration towards the low-pressure region.

If an external melt is 'pumped' into this system, it replaces the primary one, but is not in equilibrium with the surrounding solid framework. It reacts with it, and this is the 'reactive melt percolation', which enables the solid minerals of the framework to change their composition. The volume of interconnected interstitial channels does not need to be high in order to enable a large time-integrated volume of migrating melt to pass through. The new mineral compositions originate by replacement of the former ones, and at high melt/rock ratios under equilibrium conditions the minerals acquire the characteristics of the melt. This enables calculating metasomatizing melt composition from mineral composition, as is conventionally done in mantle xenolith studies (e.g. Aulbach et al., 2013). Moreover, if this kind of system is cooled, additional clinopyroxene and spinel crystallize from solidifying melt (Fig. 13). This may also explain the higher average sulfide modal abundances in the strongly melt-metasomatized Group I lherzolites, given that refertilization is frequently accompanied by sulfide saturation, which co-precipitates with spinel (Wittig et al., 2010).

Relationship between group I lherzolites and group A websterites in the Oku mantle lithosphere: Channelized vs. intergranular flow of basaltic melt

The fabric of two lherzolites belonging to Group I (H42, H46) is characterized by discordant crystallographic orientation of both ortho-and clinopyroxene relative to the olivine framework (Fig. 5). Ortho-and clinopyroxene axes are parallel to each other in these two rocks, which shows that both minerals crystallized/recrystallized during the same event and are texturally later than the olivine framework. Clinopyroxene is chemically similar in terms of REE, trace elements and $^{87}Sr/^{86}Sr$ ratio to that occurring in the websterites of Group A. Therefore, we suggest that both ortho-and clinopyroxene in the lherzolites of Group I crystallized and/or recrystallized during reactive percolation of melt which was similar to that from which websterites of Group A originated.

We suggest that the described mantle rock assemblage consisting of lherzolites of Group I and websterites of Group A was in supra-solidus conditions. The lherzolites were formed by intergranular reactive percolation of melt, whereas the websteritic accumulations result from migration of the same melt in channels. The flat, HREE-rich portions of clinopyroxene REE patterns suggest that melt generation and percolation occurred in the spinel stability field, as discussed for websterites above. The sequence of events, comprising melting followed by melt metasomatism, was proposed for nearby Lake Nyos lherzolites by
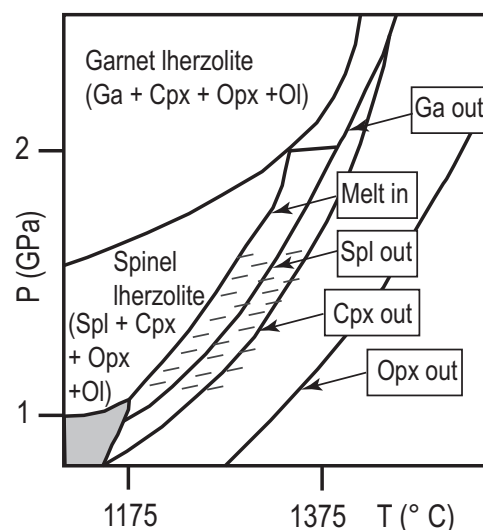

Fig. 13. Semi-quantitative phase diagram showing melting relations of lherzolite KLB-1 (based on diagram of Jennings & Holland, 2015), which is similar to the lherzolites of Group I in terms of mineral compositions (cf. Davis et al., 2009). The area of plagioclase lherzolite is marked grey. The area of incipient melting necessary for melt percolation is dashed. The volume of melt generated from spinel lherzolite between solidus and clinopyroxene-out line is from few to max. 20 vol.% (Jennings & Holland, 2015).

Liu et al. (2020), who obtained a Lu-Hf isochron at ~2.0 Ga. This date may also apply to reactive melt percolation described in this study. In contrast, the age of the original melt depletion event remains subject to interpretation.

Relationships between lherzolites of group I and group Ia

The temperatures recorded in Group I xenoliths (910–973°C) cover around 5 km of the depth profile (Fig. 11). Similar temperatures are recorded in xenoliths H41, H55 and HX2 of Group Ia. This suggests that these rocks come from the same part of mantle section if they equilibrated to the same geotherm.

The minerals of Group Ia lherzolites H41, H55 and HX2 show small, gradually varying differences (Table 2, Figs. 6, 7, 8, 9, 10). Their clinopyroxene MREE/HREE patterns (Table 1, Fig. 9) are identical to those of Group I clinopyroxene, whereas the LREE are less depleted and variable (Fig. 9). The $^{87}Sr/^{86}Sr$ ratios of 0.7021 to 0.7025 are higher than those of Group I (0.7017 to 0.7020; Fig. 10). This variation is analogous to that occurring in the Lherz lherzolites close to their contact with harzburgitic protolith (Le Roux et al., 2007, 2008). Therefore, we suggest that lherzolites H41, H55 and HX2 of Group Ia come from marginal parts of refertilized masses of Group I.

Crystal-preferred orientation results show that lherzolite HX1, which is most strongly enriched in LREE (Fig. 9), contains ortho- and clinopyroxene with crystallographic axes parallel to each other and both oriented at a low angle to olivine (Fig. 5). This suggests a consistent fabric reflecting a single deformation event which affected all phases. The Sr content of clinopyroxene (295 $\mu g/g$) suggests involvement of silicate melts in which incompatible elements are strongly enriched (the ratios of Ti/Eu = 3956 and La_N/Yb_N = 0.38 exclude carbonatitic metasomatism, Coltorti et al., 1999). By analogy with the Lherz massif, we suggest that this lherzolite represents a cryptic metasomatism front preceding the – but not affected by – the melting and melt percolation which shaped Group I lherzolites.

Lherzolite H47 has an olivine-orthopyroxene framework of consistent crystal-preferred orientation, in which clinopyroxene probably crystallized later (Fig. 5) because its crystallographic axes display a slightly different orientation to olivine and orthopyroxene ([001] axes at ∼45° to X). The temperature of ortho- and clinopyroxene equilibration suggest that this lherzolite comes from below the level of Group I lherzolites. The clinopyroxene in this rock has LREE compositions which vary at the section scale (see Fig. 9 and *Mineral chemistry of lherzolites*). The temperatures of equilibration of pyroxene margins are higher than those recorded in grain centers and in REE exchange (Electronic Supplementary Material 8). The Ca content in olivine (590–790 ppm) is relatively high, and the Cr# of spinel (0.14) is also higher than that of the majority of Groups I and Ia lherzolites (Fig. 6b, Fig. 8a, Table 2). This, together with the high $^{87}Sr/^{86}Sr$ ratio of 0.7028, suggests that this rock is transitional between Group I and II lherzolites. Therefore, we suggest that lherzolite H47, although preserving many features of Group I, was subjected to a short melt metasomatic overprint which was similar to that which affected Group II lherzolites, but less intense.

Origin of lherzolites of group II and group III

The thermo-stratigraphic relationships (Fig. 11) suggest that the lherzolites of Groups II and III occur at mantle levels different from lherzolites of Group I and Ia, and therefore probably evolved independently.

The lherzolites of Group II. These rocks are characterized by LREE-enriched patterns in clinopyroxene which have high Sr abundances (ca. 230 μg/g) and $^{87}Sr/^{86}Sr = 0.7033$. The coexisting spinel has high Cr# (0.28–0.29). The geothermometric calculations indicate temperatures in excess of 1000–1100°C, placing these two rocks in the deep part of 'stratigraphic' sequence of the Wum profile (Fig. 11).

One example of this Group of rocks, lherzolite H64, exhibits a slight shift of orthopyroxene [001] axes relative to those of olivine [100], similar to orthopyroxene from sample HX1 from Group Ia. However, orthopyroxene [100] and [010] axes from H64 sample are more dispersed than in the transitional HX1 sample. Moreover, in sample H64 clinopyroxene axes display only a weak point concentration on [010] at 45° to Z, and this clinopyroxene is undeformed and occurs in the interstices. These observations suggest that it crystallized without strain, and after orthopyroxene. High Sr contents in clinopyroxene suggest metasomatism by a small-volume, highly alkaline melt. Indeed, the clinopyroxene $(La/Yb)_N$ vs. Ti/Eu values (H63: 7.2 vs. 2445, H64: 5.4 vs. 3110) are again typical for silicate melt rather than carbonatite metasomatism (Coltorti *et al.,* 1999). The $^{87}Sr/^{86}Sr$ ratios of clinopyroxene correspond to values occurring in the lavas of the OVG (Asaah *et al.,* 2021). However, the REE contents of hypothetical melts calculated from clinopyroxene are much richer in LREE than the lavas. Therefore, Group II lherzolites may record precursory metasomatism by a small-volume alkaline melt occurring close to the recent LAB, which possibly is broadly coeval with the volcanism in the OVG.

The lherzolites of Group III. Group III comprises lherzolites which are olivine-rich (72–78 vol.%), strongly aluminum-depleted, have depleted Sr isotopic signatures ($^{87}Sr/^{86}Sr = 0.7021$), and have consistent fabric of all phases (representative example H53). The rocks of Group III come from shallow levels of the lithospheric mantle beneath Oku (Fig. 11) and their high olivine and low pyroxene content would be consistent with higher degrees of

melt depletion related to ancient melting. Therefore, Group III lherzolites plausibly were the protolith for Group I lherzolites and predate them. Group III lherzolites may represent the sub-Moho layer which was not included in the evolution of deeper-seated parts of lithospheric mantle.

Significance of spinel compositions

The datapoints representing spinel from group A websterites (H43, H65 and H50) plot close to the Primitive Upper Mantle (PUM) composition in the diagram of Fo in olivine vs. Cr# in spinel (Fig. 8b). This is consistent with the interpretation that the parental melts of websterites originated from low degrees of melting of asthenosphere. Conversely, the points representing most of the lherzolites fall on the PUM melting line (Fig. 8). As these lherzolites originated by refertilization of a protolith similar to group III (H13 and H53) by parental melts of the websterites, the arrangement of points is interpreted to reflect different degrees of refertilization, not depletion. The fluid-metasomatized amphibole-bearing lherzolite H69 and two lherzolites constituting group III, which originated by metasomatism by alkaline melts similar to those of the CVL, depart from the melting-refertilization trend (Fig. 8b). Thus, the different origins of the various groups of xenoliths are also captured by their spinel compositions.

Befang vs Wum xenolith suites

The Group I and II lherzolites from Befang and Wum were defined on the basis of clinopyroxene REE patterns. Thus, all the Group I lherzolites contain LREE depleted clinopyroxene (Tedonkenfack *et al.,* 2021). The Group I lherzolites from Befang consist of an olivine-orthopyroxene framework to which clinopyroxene and spinel were added and thus do not match its fabric. The clinopyroxene from lherzolite BFA28 ($^{87}Sr/^{86}Sr = 0.7018$) shows a chaotic crystallographic arrangement of [001] axes and that from BFA43 ($^{87}Sr/^{86}Sr = 0.7019$) shows weak concentration close to Y (Tedonkenfack *et al.,* 2021). The clinopyroxene from lherzolite BFA17 ($^{87}Sr/^{86}Sr = 0.7024$ which locates it in the Group Ia) has [001] axes parallel to Z. Nevertheless, the Group I lherzolites from Befang exhibit only clinopyroxene and spinel addition/recrystallization, whereas some of those from Wum exhibit also orthopyroxene addition/recrystallization. Thus, Befang lherzolites are suggested to show a smaller departure from the solidus in P–T space compared with those from Wum.

The lherzolites of Group II in Befang consist of olivine, ortho- and clinopyroxene sharing the same fabric. The clinopyroxenes occurring in this Group have LREE-enriched patterns. The lherzolites of Group II were considered by Tedonkenfack *et al.* (2021) to represent the protolith of Group I, whereas we here recognize the more depleted Group III lherzolites as the protolith. The Befang xenolith suite described by Tedonkenfack *et al.* (2021) comes almost entirely from the mantle section affected by MORB-like melt infiltration, and the xenoliths of Group II correspond to the Group Ia defined in this study for Wum xenolith suite. Indeed, many xenoliths from Befang have $^{87}Sr/^{86}Sr$ ratios between 0.7022 and 0.7025, placing them in Group Ia.

Almost all Befang xenoliths record a narrow range of temperatures (951–992°C; Table 3). Because T_{BK} and T_{REE} are similar, we suggest that they are representative for steady state geotherms at the moment of xenolith entrainment. Thus, the Befang xenoliths represent a narrower part of the mantle profile than those from Wum (Fig. 11).
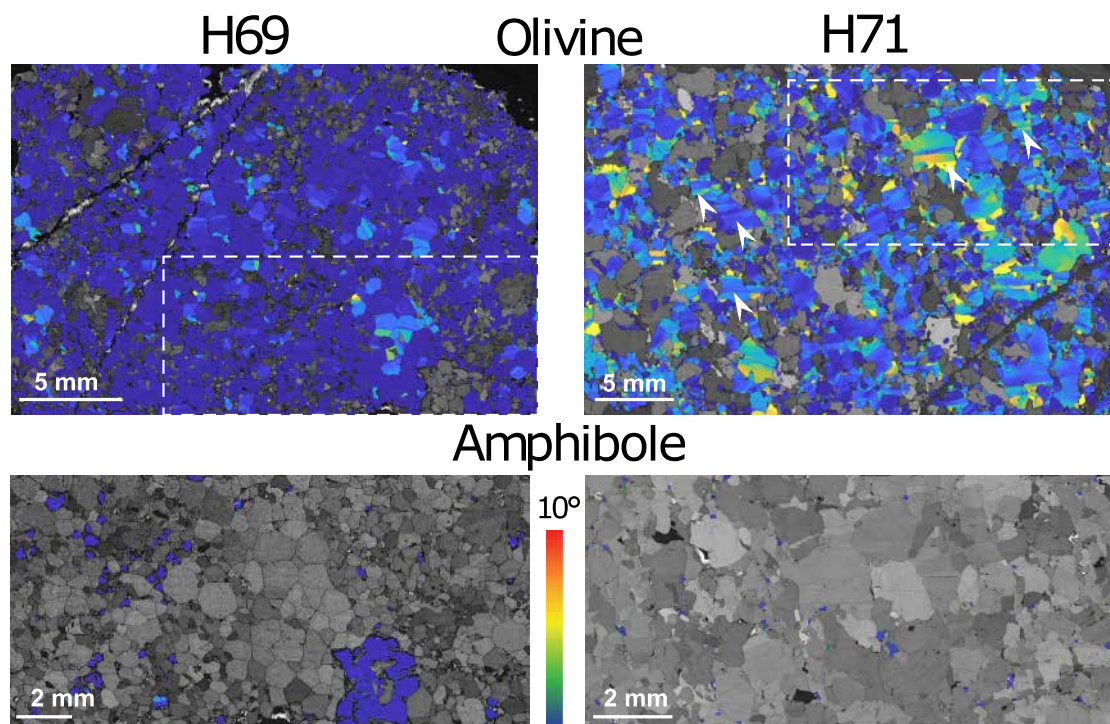
Fig. 14. Misorientation maps of amphibole-bearing lherzolites H71 and H69.

The effects of hydrous fluid percolation: Recrystallization and amphibole growth

Three lherzolites of the studied suite (H46, H71 and H69) contain amphibole. Lherzolite H46 contains few small, individual amphibole grains (0.1 vol.%). Sparse, small grains of interstitial amphibole occur in H71, whereas H69 contains asymmetric aggregates and streaks of the mineral resembling the extensional S-C fabric (Fig. 4ef). Texturally, amphibole post-dates the rest of the minerals in both H69 and H71. In all lherzolites (H46, H71 and H69), the grains of amphibole do not display internal deformation. The lherzolites H46 and H71 share the characteristics of other lherzolites from Group I in terms of major and trace elements composition of minerals, including Sr content (58–81 μg/g, Electronic Supplementary Material 2) and ^{87}Sr/^{86}Sr ratio of clinopyroxene (0.7017 and 0.7018, Table 2). The amphibole from lherzolite H71 has a LREE-depleted pattern characteristic for Group I. In contrast to other lherzolites of Group I, the ortho- and clinopyroxene CPOs are concordant to that of olivine ($(001)_{cpx}$ and $(001)_{opx}$ parallel to $(100)_{ol}$) in the lherzolite H71, indicating coherent fabric evolution. Olivine records strong plastic deformation (numerous low-angle boundaries and a shape-preferred orientation), whereas the degree of internal deformation of orthopyroxene and clinopyroxene, visible in larger grains, is lower (Fig.). The mineral chemical composition suggests that lherzolite H71 was subjected to a melt percolation event similar to that which affected other rocks of Group I, but subsequently was subjected to recrystallization during migration of hydrous fluid. More advanced stages of that process are possibly recorded in lherzolite H69, the fabric of which shows complete recrystallization and mineral compositions are changed.

The amphibole in H46 and H71 is enriched in Ti relative to that in H69 (TiO$_2$ = 2.5–2.7 vs. 0.6 wt.%) and depleted in Cr (Cr$_2$O$_3$ = 1.0 vs. 1.7 wt.%, see Electronic Supplementary Material 1). The composition of minerals in lherzolite H69 is different from any other lherzolite from the suite and the rock is classified as a separate type (Table 2). The REE patterns of both clinopyroxene and amphibole are LREE-enriched. The two minerals have ^{87}Sr/^{86}Sr ratios (0.7027 and 0.7031, respectively) which are high relative to those of clinopyroxene from other rocks of the Wum xenolith suite (Table 2). The lherzolite H69 shows strong post-tectonic recrystallization with all olivine crystals texturally re-equilibrated and grain boundaries forming triple junctions at 120° (Fig. 14).

The lherzolites H46 and H71 represent a snapshot of the early stages of amphibole formation in the Oku lherzolites. The mineral is sparse and the host rock is chemically not markedly affected. The lherzolite H69 shows advanced stages of amphibole formation: amphibole is abundant, the minerals of the host are recrystallized and their chemical and isotopic composition is changed relative to other lherzolites of the Wum xenolith suite.

Comparison to other amphibole-bearing lherzolites from Oku

Amphibole-bearing lherzolites occur in other xenolith suites found in the Oku Volcanic Group. Lee *et al.* (1996) describe spinel lherzolite C271D with a small amount of fine ($\leq$ 0.1 mm) amphibole from Lake Enep (see Fig. 1 for location of sites). The major element compositions of minerals from this lherzolite are similar to those of H69 lherzolite in this study, except amphibole, which contains slightly more titanium (1.2 wt.% of TiO$_2$) and no potassium. The analysis of clinopyroxene concentrates from xenolith C271D (Lee *et al.*, 1996) yielded an ^{87}Sr/^{86}Sr ratio 0.703074 ± 10, also broadly similar to H69 (0.7027 in clinopyroxene and 0.7031 in amphibole), and we assume that both rocks were chemically re-equilibrated during the amphibole-forming event. The model Nd age of clinopyroxene from C271D is ca 200 Ma, suggesting that amphibole was added to Oku lithospheric mantle at the time of Atlantic opening (for further discussion see Lee *et al.*, 1996).

Temdjim (2012) found 3 amphibole-bearing lherzolites, 2 harzburgites and an olivine websterite at Lake Nyos. All of them contain small volumes ($\leq$ 1 vol.%) of interstitial 1–2 mm brown
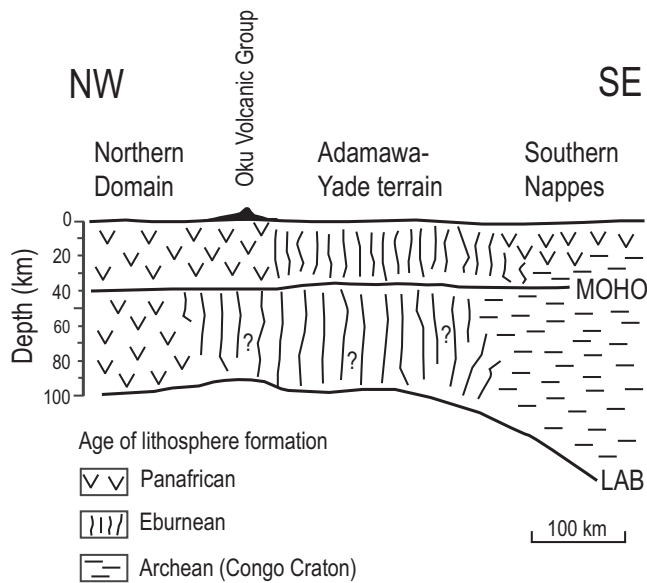
Fig. 15. Schematic NW-SE cross-section showing the probable extent of various kinds of mantle lithosphere relative to major crustal lithological units in Cameroon. Question marks in the deeper part of the lithosphere indicate uncertainty regarding the age of the protolith prior to ca. 2 Ga (Eburnean) refertilization.

amphibole grains. Pintér *et al.* (2015) described two amphibole-bearing lherzolites with 1 vol.% of 0.3–0.8 mm interstitial grains of amphibole from Lake Nyos. The amphibole described by these authors has a composition similar to that in this study. The major element variation described by Temdjim (2012) is slightly broader (TiO_2 0.3–3.2 wt.%, Cr_2O_3 1.0–2.3 wt.% except olivine websterite 0.6 wt.%).

The cited studies show that small amounts of amphibole occur in a significant part of the peridotite xenoliths occurring in the Oku Volcanic Group. They also show that amphibole post-dates the fabric defined by major rock-forming minerals, and its variable composition may reflect the effects of small-scale interaction of hydrous fluid with the peridotite matrix in a dominantly rock- rather than fluid-buffered system.

Crust–mantle decoupling beneath Oku mantle lithosphere and the meaning of Eburnean ages

The clinopyroxene occurring in Group I lherzolites and Group A websterites was formed by percolation of MORB-like melt (see above). Its $^{87}Sr/^{86}Sr$ ratios indicate Paleoproterozoic melt extraction from a convecting mantle source at ∼2.0–2.25 Ga. This age matches a suggested mantle lithosphere depletion event at ∼2.0 Ga indicated by both Re-Os and Lu-Hf isotope systematics (J. Liu *et al.*, 2020) and 2.07–2.08 Ga ages recorded in crustal rocks of the Adamawa-Yade terrain (Tchakounté *et al.*, 2017). On the other hand, the ∼2.0–2.25 Ga age does not fit the Neoproterozoic age of the crystalline basement of the Northern Domain, which underlies the OVG (see *Crust and lithospheric mantle underlying CVL*). Because the Adamawa-Yade terrain is located to the SSE of the OVG (Fig. 1), this may indicate that the Paleoproterozoic mantle lithosphere continues to the NW under the Neoproterozoic crust formed during Panafrican orogeny (Fig. 15). Such crust–mantle decoupling in orogens is quite common, and has been documented in the Central Asian Orogenic Belt and elsewhere (Lin *et al.*, 2022). The origin of the Adamawa-Yade terrain and

its link to the SCLM underneath the OVG are uncertain. Their similar ages may reflect a common origin either via *in-situ* formation during the Eburnean subduction and collision at the northern edge of the Congo craton (e.g. Tchouankoue *et al.*, 2021; Stern, 2023) or as complementary crust and lithospheric mantle of a Paleoproterozoic microcontinent (Nkoumbou *et al.*, 2014). Alternatively, the SCLM underlying the OVL may represent cratonic lithosphere that was strongly reworked during the Eburnean orogeny, an interpretation that gains some support from Archean model ages reported for OVL xenoliths by Liu *et al.* (2017). Because all model ages are subject to assumptions, and even isochron ages may reflect isotopic resetting during major refertilization rather than original melt depletion ages, the age of the harzburgitic protolith remains a matter of interpretation, but a minimum age of ca. 2.0 Ga can be safely assumed.

CONCLUSIONS

We collected mineral major and trace element data as well as clinopyroxene Sr isotope compositions and crystal preferred orientation data in order to elucidate the origin and thermo-chemical evolution of SCLM beneath the Oku Volcanic Group in Cameroon and gain insights into the mechanisms responsible for the formation of fertile, DMM-like continental lithosphere. These data show that a significant part of the mantle lithosphere beneath Oku consists of secondary lherzolites (Group I) which compositionally resemble the DMM *sensu* Workman & Hart (2005). Group I lherzolites originated metasomatically by intergranular reactive percolation of MORB-like melts in a lherzolitic protolith at spinel-facies conditions. The protolith was partially molten under conditions slightly above its solidus. Group III lherzolites may represent the protolith little affected by melt percolation, whereas Group Ia lherzolites represent a transitional lithology presumably occurring at the margins of rejuvenated Group I lherzolites. The percolating melt formed also channels, which are documented by websterites of Group A. This melt was generated in the spinel-facies and did not evolve to strongly depleted compositions typical for advanced stages of melting in oceanic rifts. Subsequently, a separate event affected the Oku mantle lithosphere, locally adding small amounts of amphibole.

The Cenozoic CVL volcanism had little effect on the Oku mantle lithosphere. The sparse websterites of Group C precipitated from ascending alkaline lavas, but little metasomatic modification of mantle peridotites occurred, with the possible exception of the of Group II lherzolites, which are suggested to derive from near the LAB on account of their higher equilibrium temperatures.

The $^{87}Sr/^{86}Sr$ ratios of clinopyroxene in Group I lherzolites and Group A websterites, which precipitated from the migrating MORB-like melt, indicate Paleoproterozoic formation at ∼2.0–2.25 Ga. This age coincides with a lithospheric mantle depletion or reworking event at ∼2.0 Ga indicated by Re-Os and Lu-Hf isotope systematics of xenoliths from the OVG (Liu *et al.*, 2020) and with 2.07–2.08 Ga ages recorded in crustal rocks of the Adamawa-Yade terrain (Tchakounté *et al.*, 2017), but does not match the Neoproterozoic age of the crystalline basement of Northern Domain which underlies the OVG. Since the Adamawa-Yade terrain is located to the SSE of the Oku Volcanic Group, this may indicate that the Paleoproterozoic (Eburnean) mantle lithosphere continues to the NW under the Neoproterozoic (Cryogenian – Ediacaran) crust formed during the Panafrican orogeny (Fig. 15).

SUPPLEMENTARY MATERIAL

Supplementary data are available at *Journal of Petrology* online.

DATA AVAILABILITY

Analytical data underlying this paper are available in the paper and in its online supplementary material.

References

Abdelsalam, M. G., Liégeois, H.-P. & Stern, R. J. (2002). The Saharan Metacraton. *Journal of African Earth Sciences* **34**, 119–136. https://doi.org/10.1016/S0899-5362(02)00013-1.

Adam, J. & Green, T. (2006). Trace element partitioning between mica- and amphibole-bearing garnet lherzolite and hydrous basanitic melt: 1. Experimental results and the investigation of controls on partitioning behaviour. *Contributions to Mineralogy and Petrology* **152**, 1–17. https://doi.org/10.1007/s00410-006-0085-4.

Alard, O., Griffin, W. L., Lorand, J. P., Jackson, S. E. & O'Reilly, S. Y. (2000). Non-chondritic distribution of the highly siderophile elements in mantle sulphides. *Nature* **407**, 891–894. https://doi.org/10.1038/35038049.

Asaah, A. N. E., Yokoyama, T., Aka, F. T., Usui, T., Kuritani, T., Wirmvem, M. J., Iwamori, H., Fozing, E. M., Tamen, J., Mofor, G. Z., Ohba, T., Tanyileke, G. & Hell, J. V. (2015). Geochemistry of lavas from maar-bearing volcanoes in the Oku volcanic Group of the Cameroon Volcanic Line. *Chemical Geology* **406**, 55–69. https://doi.org/10.1016/j.chemgeo.2015.03.030.

Asaah, A. N. E., Yokoyama, T., Iwamori, H., Aka, F. T., Kuritani, T., Usui, T., Tamen, J., Gountié Dedzo, M., Chako-Tchamabé, B., Hasegawa, T., Nche, L. A. & Ohba, T. (2021). High–μ signature in lavas of Mt. Oku: implications for lithospheric and asthenospheric contributions to the magmatism of the Cameroon Volcanic Line (West Africa). *Lithos* **400-401**, 106416. https://doi.org/10.1016/j.lithos.2021.106416.

Aulbach, S., Griffin, W. L., Pearson, N. J. & O'Reilly, S. Y. (2013). Nature and timing of metasomatism in the stratified mantle lithosphere beneath the central slave craton (Canada). *Chemical Geology* **352**, 153–169. https://doi.org/10.1016/j.chemgeo.2013.05.037.

Aulbach, S., Gerdes, A. & Viljoen, K. S. (2016). Formation of diamondiferous kyanite-eclogite in a subduction melange. *Geochimica et Cosmochimica Acta* **179**, 156–176. https://doi.org/10.1016/j.gca.2016.01.038.

Bachmann, F., Hielscher, R. & Schaeben, H. (2010). Texture analysis with MTEX – free and open source software toolbox. *Solid State Phenomena* **160**, 63–68. https://doi.org/10.4028/www.scientific.net/SSP.160.63.

Bachmann, F., Hielscher, R. & Schaeben, H. (2011). Grain detection from 2d and 3d EBSD data – specification of the MTEX algorithm. *Ultramicroscopy* **111**, 1720–1733. https://doi.org/10.1016/j.ultramic.2011.08.002.

Bodinier, J.-L. & Godard, M. (2003) Orogenic, ophiolitic and abyssal peridotites. In: Holland H. D. & Turrekian K. K. (eds) *Treatise on Geochemistry*. Elsevier, Amsterdam: The Netherlands 2, pp.103–170.

Bodinier, J.-L., Menzies, M. A., Shimizu, N., Frey, F. A. & McPherson, E. (2004). Silicate, hydrous and carbonate metasomatism at Lherz, France: contemporaneous derivatives of silicate melt-harzburgite reaction. *Journal of Petrology* **45**, 299–320. https://doi.org/10.1093/petrology/egg107.

Bodinier, J.-L., Garrido, C., Chanefo, I., Bruguier, O. & Gervilla, F. (2008). Origin of pyroxenite-peridotite veined mantle by refertilization reactions: evidence from the Ronda peridotite (southern Spain). *Journal of Petrology* **49**, 999–1025. https://doi.org/10.1093/petrology/egn014.

Bouyo, M. H., Zhao, Y., Penaye, J., Zhang, S. H. & Njel, U. O. (2015). Neoproterozoic subduction-related metavolcanic and metasedimentary rocks from the Rey Bouba Greenstone Belt of north-Central Cameroon in the Central African Fold Belt: new insights into a continental arc geodynamic setting. *Precambrian Research* **261**, 40–53. https://doi.org/10.1016/j.precamres.2015.01.012.

Brey, G. P. & Köhler, T. (1990). Geothermobarometry in four-phase lherzolites II. New thermobarometers and practical assessment of existing thermobarometers. *Journal of Petrology* **31**, 1353–1378. https://doi.org/10.1093/petrology/31.6.1353.

Bunge, H.-J. (1982) *Texture Analysis in Materials Science: Mathematical Methods*. Elsevier.

Carlson, R. W. & Ionov, D. A. (2019). Compositional characteristics of the MORB mantle and bulk silicate earth based on spinel peridotites from the Tariat region, Mongolia. *Geochimica et Cosmochimica Acta* **257**, 206–223. https://doi.org/10.1016/j.gca.2019.05.010.

Cawood, P. A., Martin, E. L., Murphy, J. B. & Pisarevsky, S. A. (2021). Gondwana's interlinked peripheral orogens. *Earth and Planetary Science Letters* **568**, 117057. https://doi.org/10.1016/j.epsl.2021.117057.

Coltorti, M., Bonadiman, C., Hinton, R. W., Siena, F. & Upton, B. G. J. (1999). Carbonatite metasomatism of the oceanic upper mantle: evidence from clinopyroxenes and glasses in ultramafic xenoliths of Grande Comore, Indian Ocean. *Journal of Petrology* **40**, 133–165. https://doi.org/10.1093/petroj/40.1.133.

Craig, J. R. (1973). Pyrite-pentlandite assemblages in the Fe-Ni-S system. *American Journal of Science* **273A**, 496–510.

Craig, J. R. & Kullerud, G. (1969). Phase relations and mineral assemblages in the copper-lead-sulfur system. *American Mineralogist* **53**, 145–161.

Davis, F. A., Tangeman, J. A., Tenner, T. J. & Hirschmann, M. M. (2009). The composition of KLB-1 peridotite. *American Mineralogist* **94**, 176–180. https://doi.org/10.2138/am.2009.2984.

Déruelle, B., Ngounouno, I. & Demaiffe, D. (2007). The 'Cameroon hot line' (CHL): A unique example of active alkaline intraplate structure in both oceanic and continental lithospheres.

Comptes Rendus Geoscience **339**, 589–600. https://doi.org/10.1016/j.crte.2007.07.007.

Fishwick, S. (2010). Surface wave tomography: imaging of the lithosphere–asthenosphere boundary beneath central and southern Africa? *Lithos* **120**, 63–73. https://doi.org/10.1016/j.lithos.2010.05.011.

Fitton, J. G. (1980). The Benue Trough and Cameroon Line: a migrating rift system in West Africa. *Earth and Planetary Science Letters* **51**, 132–138. https://doi.org/10.1016/0012-821X(80)90261-7.

Gale, A., Dalton, C. A., Langmuir, C. H., Su, Y. & Schilling, J.-G. (2013). The mean composition of ocean ridge basalts. *Geochemistry, Geophysics, Geosystems* **14**, 489–518. https://doi.org/10.1029/2012GC004334.

Gallacher, R. J. & Bastow, I. D. (2012). The development of magmatism along the Cameroon volcanic line: evidence from teleseismic receiver functions. *Tectonics* **31**, TC3018. https://doi.org/10.1029/2011TC003028.

Goussi Ngalamo, J. F., Bisso, D., Abdelsalam, M. G., Atekwana, E. A., Katumwehe, A. B. & Ekodeck, G. E. (2017). Geophysical imaging of metacratonization in the northern edge of the Congo craton in Cameroon. *Journal of African Earth Sciences* **129**, 94–107. https://doi.org/10.1016/j.jafrearsci.2016.12.010.

Goussi Ngalamo, J. F., Bisso, D., Abdelsalam, M. G., Atekwana, E. A., Katumwehe, A. B. & Ekodeck, G. E. (2018). Lithospheric structure beneath the Central Africa Orogenic Belt in Cameroon from the analysis of satellite gravity and passive seismic data. *Tectonophysics* **745**, 326–337. https://doi.org/10.1016/j.tecto.2018.08.015.

Hasterok, D. & Chapman, D. S. (2011). Heat production and geotherms for the continental lithosphere. *Earth and Planetary Science Letters* **307**, 59–70. https://doi.org/10.1016/j.epsl.2011.04.034.

Hauri, E. H. (1997). Melt migration and mantle chromatography, 1: simplified theory and conditions for chemical and isotopic decoupling. *Earth and Planetary Science Letters* **153**, 1–19. https://doi.org/10.1016/S0012-821X(97)00157-X.

Hawthorne, F. C., Oberti, R. L., Harlow, G. E., Maresch, W. V., Martin, R. F., Schumacher, J. C. & Welch, M. D. (2012). Nomenclature of the amphibole supergroup. *American Mineralogist* **97**, 2031–2048. https://doi.org/10.2138/am.2012.4276.

Henry, H., Kaczmarek, M.-A., Ceuleneer, G., Tilhac, R., Griffin, W. L., O'Reilly, S. Y., Grégoire, M. & Le Sueur, E. (2021). The microstructure of layered ultra-mafic cumulates: case study of the bear creek intrusion, trinity ophiolite, California, USA. *Lithos* **388-389**, 106047. https://doi.org/10.1016/j.lithos.2021.106047.

Holness, M. B., Vukmanovic, Z. & Mariani, E. (2017). Assessing the role of compaction in the formation of adcumulates: a microstructural perspective. *Journal of Petrology* **58**, 643–673. https://doi.org/10.1093/petrology/egx037.

Holtzman, B. K., Groebner, N. J., Zimmerman, M. E., Ginsberg, S. B. & Kohlstedt, D. L. (2003). Stress-driven melt segregation in partially molten rocks. *Geochemistry, Geophysics, Geosystems* **4**(5), 8607. https://doi.org/10.1029/2001GC000258.

Jennings, E. S. & Holland, T. J. B. (2015). A simple thermodynamic model for melting of peridotite in the system NCFMASOCr. *Journal of Petrology* **56**, 869–892. https://doi.org/10.1093/petrology/egv020.

Jochum, K. P., Weis, U., Stoll, B., Kuzmin, D., Yang, Q., Raczek, I., Jacob, D. E., Stracke, A., Birbaum, K., Frick, D. A., Günther, D. & Enzweiler, J. (2011). Determination of reference values for NIST SRM 610 – 617 glasses following ISO guidelines. *Geostandards and Geoanalytical Research* **35**, 397–429. https://doi.org/10.1111/j.1751-908X.2011.00120.x.

Kaczmarek, M.-A., Bodinier, J.-L., Bosch, D., Tommasi, A., Dautria, J.-M. & Kechid, S. A. (2016). Metasomatized mantle xenoliths as a record of the lithospheric mantle evolution of the northern edge of the Ahaggar swell, in Teria (Algeria). *Journal of Petrology* **57**, 345–382. https://doi.org/10.1093/petrology/egw009.

Kaneda, H., Takenouchi, S. & Shoji, T. (1986). Stability of pentlandite in the Fe-Ni-co-S system. *Mineralium Deposita* **21**, 169–180. https://doi.org/10.1007/BF00199797.

Kelly, D. P. & Vaughan, D. J. (1983). Pyrrhotine-pentlandite ore textures: a mechanistic approach. *Mineralogical Magazine* **47**, 453–463. https://doi.org/10.1180/minmag.1983.047.345.06.

Kullerud, G. (1963). Thermal stability of pentlandite. *Canadian Mineralogist* **7**, 353–366.

Kullerud, G. & Yoder, H. S. (1959). Pyrite stability relations in the Fe-S system. *Economic Geology* **54**, 533–572. https://doi.org/10.2113/gsecongeo.54.4.533.

Kullerud, G., Yund, R. A. & Moh, G. H. (1969) Phase relations in the Cu-Fe-S, Cu-Ni-S, and Fe-Ni-S systems. In: Wilson H. D. B. (ed) *Magmatic Ore Deposits*. Economic Geology Monograph 4, pp. 232–243.

Le Roux, V., Bodinier, J.-L., Tommasi, A., Alard, O., Dautria, J.-M., Vauchez, A. & Riches, A. J. V. (2007). The Lherz spinel lherzolite: Refertilized rather than pristine mantle. *Earth and Planetary Science Letters* **259**, 599–612. https://doi.org/10.1016/j.epsl.2007.05.026.

Le Roux, V., Bodinier, J.-L., Alard, O., O'Reilly, S. Y. & Griffin, W. L. (2009). Isotopic decoupling during porous melt flow: A case-study in the Lherz peridotite. *Earth and Planetary Science Letters* **279**, 79–85.

Lee, D.-C., Halliday, A. N., Davies, G. R., Essene, E. J., Fitton, J. G. & Temdjim, R. (1996). Melt enrichment of shallow depleted mantle: a detailed petrological, trace element and isotopic study of mantle-derived xenoliths and megacrysts from the Cameroon line. *Journal of Petrology* **37**, 415–441. https://doi.org/10.1093/petrology/37.2.415.

Lenoir, X., Garrido, C. J., Bodinier, J.-L. & Dautria, J.-M. (2000). Contrasting lithospheric mantle domains beneath the Massif Central (France) revealed by geochemistry of peridotite xenoliths. *Earth and Planetary Science Letters* **181**, 359–375. https://doi.org/10.1016/S0012-821X(00)00216-8.

Lenoir, X., Garrido, C. J., Bodinier, J.-L., Dautria, J.-M. & Gerilla, F. (2001). The recrystallization front in the Ronda peridotite: evidence for melting and thermal erosion of subcontinental lithospheric mantle beneath the Alboran Basin. *Journal of Petrology* **42**, 141–158. https://doi.org/10.1093/petrology/42.1.141.

Li, X.-H., Chen, Y., Tchouankoue, J. P., Liu, C.-Z., Li, J., Ling, X.-X., Tang, G.-Q. & Liu, Y. (2017). Improving geochronological framework of the Pan-African orogeny in Cameroon: new SIMS zircon and monazite U-Pb age constraints. *Precambrian Research* **294**, 307–321. https://doi.org/10.1016/j.precamres.2017.04.006.

Li, X., Zhang, C., Behrens, H. & Holtz, F. (2020). Calculating amphibole formula from electron microprobe analysis data using a machine learning method based on principal components regression. *Lithos* **362-363**, 105469. https://doi.org/10.1016/j.lithos.2020.105469.

Liang, Y., Sun, C. & Yao, L. (2013). A REE-in-two-pyroxene thermometer for mafic and ultramafic rocks. *Geochimica et Cosmochimica Acta* **102**, 246–260. https://doi.org/10.1016/j.gca.2012.10.035.

Lin, A.-B., Aulbach, S., Zheng, J.-P., Cai, R., Liu, J., Xiong, Q. & Pan, S.-K. (2023). Lithospheric mantle provinces and crust-mantle decoupling beneath northeastern China: insights from peridotite xenoliths. *GSA Bulletin* **135**, 990–1008. https://doi.org/10.1130/B36338.1.

Liu, C.-Z., Yang, L.-Y., Li, X.-H. & Tchounkoue, J. P. (2017). Age and Sr-Nd-Hf isotopes of the sub-continental lithospheric mantle beneath the Cameroon volcanic line: constraints from the Nyos mantle xenoliths. *Chemical Geology* **455**, 84–97. https://doi.org/10.1016/j.chemgeo.2016.07.022.

Liu, J., Pearson, G. J., Shu, Q., Sigurdsson, H., Thomassot, E. & Alard, O. (2020). Dating post-Archean lithospheric mantle: insights from Re-Os and Lu-Hf isotopic systematics of the Cameroon Volcanic Line peridotites. *Geochimica et Cosmochimica Acta* **278**, 177–198. https://doi.org/10.1016/j.gca.2019.07.010.

Lorand, J. P. (1989). Mineralogy and chemistry of Cu-Fe-Ni sulfides in orogenic-type spinel peridotite bodies from Ariege (Northeastern Pyrenees, France). *Contributions to Mineralogy and Petrology* **103**, 335–345. https://doi.org/10.1007/BF00402920.

Lorand, J. P. & Grégoire, M. (2006). Petrogenesis of base metal sulphide assemblages of some peridotites from the Kaapvaal craton (South Africa). *Contributions to Mineralogy and Petrology* **151**, 521–538. https://doi.org/10.1007/s00410-006-0074-7.

Lusk, J. & Bray, D. M. (2002). Phase relations and the electrochemical determination of sulfur fugacity for selected reactions in the Cu–Fe–S and Fe–S systems at 1 bar and temperatures between 185 and 460°C. *Chemical Geology* **192**, 227–248. https://doi.org/10.1016/S0009-2541(02)00194-8.

Makovicky, E. & Karup-Møller, S. (1995). The system Pd-Fe-Ni-S at 900 and 725°C. *Mineralogical Magazine* **59**, 685–702. https://doi.org/10.1180/minmag.1995.059.397.11.

Marchesi, C., Garrido, C. J., Bosch, D., Bodinier, J.-L., Gervilla, F. & Hidas, K. (2013). Mantle refertilization by melts of crustal-derived garnet pyroxenite: evidence from the Ronda peridotite massif, southern Spain. *Earth and Planetary Science Letters* **362**, 66–75. https://doi.org/10.1016/j.epsl.2012.11.047.

Matusiak-Małek, M., Puziewicz, J., Ntaflos, T., Grégoire, M., Benoit, M. & Klügel, A. (2014). Two contrasting lithologies in off-rift subcontinental lithospheric mantle beneath Central Europe—the Krzeniów (SW Poland) case study. *Journal of Petrology* **55**, 1799–1828. https://doi.org/10.1093/petrology/egu042.

McDonough, W. & Sun, S. (1995). The composition of the earth. *Chemical Geology* **120**, 223–253. https://doi.org/10.1016/0009-2541(94)00140-4.

Milesi, J. P., Frizon de Lamotte, D., de Kock, G. & Toteu, F. (2010) Tectonic Map of Africa. In: *Commission for the Geological Map of the World*, 2nd edn.

Min, G. & Hou, G. (2019). Mechanism of the Mesozoic African rift system: Paleostress field modeling. *Journal of Geodynamics* **132**, 101655. https://doi.org/10.1016/j.jog.2019.101655.

Morales, L. F. G. & Tommasi, A. (2011). Composition, textures, seismic and thermal anisotropies of xenoliths from a thin and hot lithospheric mantle (Summit Lake, southern Canadian Cordillera). *Tectonophysics* **507**, 1–15. https://doi.org/10.1016/j.tecto.2011.04.014.

Naldrett, A. J. & Kullerud, G. (1967). A study of the Strathcona mine and its bearing on the origin of the nickel-copper ores of the Sudbury district, Ontario. *Journal of Petrology* **8**, 453–531. https://doi.org/10.1093/petrology/8.3.453.

Naldrett, A. J., Craig, J. R. & Kullerud, G. (1967). The central portion of the Fe-Ni-S system and its bearing on pentlandite exsolution in iron-nickel sulfide ores. *Economic Geology* **62**, 826–847. https://doi.org/10.2113/gsecongeo.62.6.826.

Niu, Y. (1997). Mantle melting and melt extraction process beneath ocean ridges: evidence from abyssal peridotites. *Journal of Petrology* **38**, 1047–1074. https://doi.org/10.1093/petroj/38.8.1047.

Niu, Y., Wilson, M., Humphreys, E. R. & O'Hara, M. J. (2011). The origin of intra-plate Ocean Island basalts (OIB): the lid effect and its geodynamic implications. *Journal of Petrology* **52**, 1443–1468. https://doi.org/10.1093/petrology/egr030.

Nixon, P. H. (1987) *Mantle xenoliths*. Chichester: Wiley, 844.

Njome, M. S. & De Wit, M. J. (2014). The Cameroon line: analysis of an intraplate magmatic province transecting both oceanic and continental lithospheres: constraints, controversies and models. *Earth-Science Reviews* **139**, 168–194. https://doi.org/10.1016/j.earscirev.2014.09.003.

Nkoumbou, C., Barbey, P., Yonta-Ngoune, C., Paquette, J. L. & Villiéras, F. (2014). Pre-collisional geodynamic context of the southern margin of the Pan-African fold belt in Cameroon. *Journal of African Earth Sciences* **99**, 245–260. https://doi.org/10.1016/j.jafrearsci.2013.10.002.

O'Reilly, S. Y. & Griffin, W. L. (2013) Mantle metasomatism. In: Harlov D. E. & Austrheim H. (eds) *Metasomatism and the Chemical Transformation of Rock. Lecture Notes in Earth Sciences*. Springer, pp.471–533.

O'Reilly, S. Y., Zhang, M., Griffin, W. L., Begg, G. & Hronsky, J. (2009). Ultradeep continental roots and their oceanic remnants: a solution to the geochemical "mantle reservoir" problem? *Lithos* **112**, 1043–1054. https://doi.org/10.1016/j.lithos.2009.04.028.

Pearson, D. G., Canil, D. & Shirey, S. B. (2003) Mantle samples included in volcanic rocks: xenoliths and diamonds. In: Holland H. D. & Turrekian K. K. (eds) *Treatise on Geochemistry*. Elsevier 2, pp.171–275.

Pearson, D. G., Canil, D. & Shirey, S. B. (2014) Mantle samples included in volcanic rocks: xenoliths and diamonds. In: Holland H. D. & Turrekian K. K. (eds) *Treatise on Geochemistry*. Elsevier3, pp.169–253.

Pintér, Z., Patkó, L., Djoukam, J. F. T., Kovács, I., Tchouankoue, J. P., Falus, G., Konc, Z., Tommasi, A., Barou, F., Mihály, J., Németh, C. & Jeffries, T. (2015). Characterization of the sub-continental lithopsheric mantle beneath the Cameroon volcanic line inferred from alkaline basalts hosted peridotite xenoliths from Barombi Mbo and Nyos Lakes. *Journal of African Earth Sciences* **111**, 170–193. https://doi.org/10.1016/j.jafrearsci.2015.07.006.

Puziewicz, J., Matusiak-Małek, M., Ntaflos, T., Grégoire, M., Kaczmarek, M.-A., Aulbach, S., Ziobro, M. & Kukuła, A. (2020). Three major types of subcontinental lithospheric mantle beneath the Variscan orogen in Europe. *Lithos* **362-363**, 105467. https://doi.org/10.1016/j.lithos.2020.105467.

Rankenburg, K. (2002) *Megacrysts in Volcanic Rocks of the Cameroon Volcanic Line—Constrains on Magma Genesis and Contamination*. Doctoral dissertation. Institut für Mineralogie. Frankfurt am Main: Goethe-Universität, p.82.

Reusch, A. M., Nyblade, A. A., Wiens, D. A., Shore, P. J., Ateba, B., Tabod, C. T. & Nnange, J. M. (2010). Upper mantle structure beneath Cameroon from body wave tomography and the origin of the Cameroon volcanic line. *Geochemistry, Geophysics, Geosystems* **11**. https://doi.org/10.1029/2010GC003200.

Salters, V. J. M. & Stracke, A. (2004). Composition of the depleted mantle. *Geochemistry, Geophysics, Geosystems* **5**, Q05B07. https://doi.org/10.1029/2003GC000597.

Scott, J. M., Liu, J., Pearson, D. G., Harris, G. A., Czertowicz, T. A., Woodland, S. J., Riches, A. J. V. & Luth, R. W. (2019). Continent stabilisation by lateral accretion of subduction zone-processed mantle residues; insights from Zealandia. *Earth and Planetary Science Letters* **507**, 175–186. https://doi.org/10.1016/j.epsl.2018.11.039.

Sobh, M., Ebbing, J., Mansi, A. H., Götze, G.-J., Emry, E. L. & Abdelsalam, M. G. (2020). The lithospheric structure if the Saharan Metacraton from 3-D integrated geophysical-petrological modelling. *Journal of Geophysical Research Solid Earth* **125**, e2019JB018747. https://doi.org/10.1029/2019JB018747.

Soustelle, V., Tommasi, A., Bodinier, J. L., Garrido, C. J. & Vauchez, A. (2009). Deformation and reactive melt transport in the mantle lithosphere above large-scale partial melting domain: the Ronda peridotite massif, southern Spain. *Journal of Petrology* **50**, 1235–1266. https://doi.org/10.1093/petrology/egp032.

Steiger, R. H. & Jäger, E. (1977). Subcommission on geochronology: convention on the use of decay constants in geo- and cosmochronology. *Earth and Planetary Science Letters* **36**, 359–362. https://doi.org/10.1016/0012-821X(77)90060-7.

Stern, R. J. (2023). The Orosirian (1800-2050 Ma) plate tectonic episode: key for reconstructing the Proterozoic tectonic record. *Geoscience Frontiers* **14**, 101553. https://doi.org/10.1016/j.gsf.2023.101553.

Sun, C. & Liang, Y. (2014). An assessment of subsolidus re-equilibration on REE distribution among mantle minerals olivine, orthopyroxene, clinopyroxene, and garnet in peridotites. *Chemical Geology* **372**, 80–91. https://doi.org/10.1016/j.chemgeo.2014.02.014.

Tchakounté, J., Eglinger, A., Toteu, S. F., Zeh, A., Nkoumbou, C., Mvondo-Ondoa, J., Penaye, J., de Wit, M. & Barbey, P. (2017). The Adamawa-Yadé domain, a piece of Archean crust in the Neoproterozoic Central African Orogenic belt (Bafia area, Cameroon). *Precambrian Research* **299**, 210–229. https://doi.org/10.1016/j.precamres.2017.07.001.

Tchouankoue, J.-P., Tchato Tchaptchet, D. P. I., Nyassa, L. M., Njuinang, J. D., Feudjou, C. M., Tchato, C. F., Ngambi, P. E. B. & Li, X.-H. (2021). Evidence for a 2.06 subduction at the western border of the Adamawa-Yade domain in Cameroon: constraints from elemental geochemistry, zircon Hf isotopes and zircon U/Pb geochronology from Ititin metabasites. *Journal of African Earth Sciences* **175**, 104001. https://doi.org/10.1016/j.jafrearsci.2020.104001.

Tedonkenfack, S. S. T., Puziewicz, J., Aulbach, S., Ntaflos, T., Kaczmarek, M.-A., Matusiak-Małek, M., Kukuła, A. & Ziobro, M. (2021). Lithospheric mantle refertilization by DMM-derived melts beneath the Cameroon volcanic line—a case study of the Befang xenolith suite (Oku Volcanic Group, Cameroon). *Contributions to Mineralogy and Petrology* **176**, 37. https://doi.org/10.1007/s00410-021-01796-3.

Temdjim, R. (2012). Ultramafic xenoliths from Lake Nyos area, Cameroon Volcanic Line, west-Central Africa: Petrography, mineral chemistry, equilibration conditions and metasomatic features. *Chemie der Erde* **72**, 39–60. https://doi.org/10.1016/j.chemer.2011.07.002.

Tommasi, A., Vauchez, A. & Ionov, D. (2008). Deformation, static recrystallization, and reactive melt transport in shallow subcontinental mantle xenoliths (Tok Cenozoic volcanic field, SE Siberia). *Earth and Planetary Science Letters* **272**, 65–77. https://doi.org/10.1016/j.epsl.2008.04.020.

Toteu, S. F., de Wit, M., Penaye, J., Drost, K., Tait, J. A., Bouyo, M. H., van Schmus, W. R., Jelsma, H., Moloto-A-Kenguemba, G. R., da Silva Finho, A. F., Lerouge, C. & Doucoure, M. (2022). Geochronology and correlations in the Central African Fold Belt along the northern edge of the Congo Craton: new insighths from U-Pb dating of zircons from Cameroon, Central African Republic, and South-Western Chad. *Gondwana Research* **107**, 296–324. https://doi.org/10.1016/j.gr.2022.03.010.

Van Achterberg, E., Ryan, C. G., Jackson, S. E. & Griffin, W. L. (2001) Data reduction software for LA-ICP-MS. In: Sylvester P. J. (ed) *Laser ablation ICPMS in the Earth sciences, Principles and Applications. Mineralogical Association of Canada, Short Course Series* 29, pp.239–243.

Van der Wal, D. & Bodinier, J. L. (1996). Origin of the recrystallization fromt in the Ronda peridotite by km-scale pervasive porous melt flow. *Contributions to Mineralogy and Petrology* **122**, 387–405. https://doi.org/10.1007/s004100050135.

Warren, J. M. (2016). Global variations in abyssal peridotite compositions. *Lithos* **248-251**, 193–219. https://doi.org/10.1016/j.lithos.2015.12.023.

Warren, J. M. & Shimizu, N. (2010). Cryptic variations in abyssal peridotite compositions: evidence for shallow-level melt infiltration in the oceanic lithosphere. *Journal of Petrology* **51**, 395–423. https://doi.org/10.1093/petrology/egp096.

Waters, C. L., Sims, W. W. K., Perfit, M. R., Blichert-Toft, J. & Blusztajn, J. (2011). Perspectove on the genesis of E-MORB from chemical and isotopic heterogeneity at 9-10 °N East Pacific rise. *Journal of Petrology* **52**, 565–602. https://doi.org/10.1093/petrology/egq091.

Witt-Eickschen, G. & O'Neill, H. S. C. (2005). The effect of temperature on the equilibrium distribution of trace elements between clinopyroxene, orthopyroxene, olivine and spinel in upper mantle peridotite. *Chemical Geology* **221**, 65–101. https://doi.org/10.1016/j.chemgeo.2005.04.005.

Wittig, N., Pearson, D. G., Baker, J. A., Duggen, S. & Hoernle, K. (2010). A major element, PGE and Re-Os isotope study of middle atlas (Marocco) peridotite xenoliths: evidence for coupled introduction of metasomatic sulfides and clinopyroxene. *Lithos* **115**, 15–26. https://doi.org/10.1016/j.lithos.2009.11.003.

Workman, R. K. & Hart, S. R. (2005). Major and trace element composition of the depleted MORB mantle (DMM). *Earth and Planetary Science Letters* **231**, 53–72. https://doi.org/10.1016/j.epsl.2004.12.005.

Yao, L., Sun, C. & Liang, Y. (2012). A parameterized model for REE distribution between low-Ca pyroxene and basaltic melts with applications to REE partitioning in low-Ca pyroxene along a mantle adiabat and during pyroxenite-derived melt and peridotite interaction. *Contributions to Mineralogy and Petrology* **164**, 261–280. https://doi.org/10.1007/s00410-012-0737-5.

Zaffarana, C., Tommasi, A., Vauchez, A. & Grégoire, M. (2014). Microstructures and seismic properties of south Patagonian mantle xenoliths (Gobernador Gregores and Pali Aike). *Tectonophysics* **621**, 175–197. https://doi.org/10.1016/j.tecto.2014.02.017.